

Stability analyses of two-temperature radiative shocks: formulation, eigenfunctions, luminosity response and boundary conditions

Curtis J. Saxton^{1,2,3} & Kinwah Wu^{1,4}

¹ School of Physics, University of Sydney, NSW 2006, Australia

² Research School of Astronomy & Astrophysics, Australian National University, ACT 0200, Australia, saxton@mso.anu.edu.au

³ Department of Theoretical Physics, Faculty of Science, Australian National University, ACT 0200, Australia

⁴ Mullard Space Science Laboratory, University College London, Holmbury St Mary, Dorking, Surrey RH5 6NT

Received:

ABSTRACT

We present a general formulation for stability analyses of radiative shocks with multiple cooling processes, longitudinal and transverse perturbations, and unequal electron and ion temperatures. Using the accretion shocks of magnetic cataclysmic variables as an illustrative application, we investigate the shock instabilities by examining the eigenfunctions of the perturbed hydrodynamic variables. We also investigate the effects of varying the condition at the lower boundary of the post-shock flow from a zero-velocity fixed wall to several alternative type of boundaries involving the perturbed hydrodynamic variables, and the variations of the emission from the post-shock flow under different modes of oscillations. We found that the stability properties for flow with a stationary-wall lower boundary are not significantly affected by perturbing the lower boundary condition, and they are determined mainly by the energy-transport processes. Moreover, there is no obvious correlation between the amplitude or phase of the luminosity response and the stability properties of the system. Stability of the system can, however, be modified in the presence of transverse perturbation. The luminosity responses are also altered by transverse perturbation.

Key words: accretion — shock waves — stars: binaries: close — stars: white dwarfs

1 INTRODUCTION

The time-dependent properties of radiative shocks have been investigated by many researchers in different settings, for example the interactions between supernova shocks and the interstellar medium, and accretion flow onto compact objects (e.g. Falle 1975, 1981; Langer, Chanmugam & Shaviv 1981, 1982; Chevalier & Imamura 1982; Imamura, Wolff & Durisen 1984; Chanmugam, Langer & Shaviv 1985; Imamura 1985; Bertschinger 1986; Innes, Giddings & Falle 1987a, b; Gaetz, Edgar & Chevalier 1988; Wolff, Gardner & Wood 1989; Imamura & Wolff 1990; Houck & Chevalier 1992; Wu, Chanmugam & Shaviv 1992; Tóth & Draine 1993; Dgani & Soker 1994; Strickland & Blodin 1995; Wu et al. 1996; Imamura et al. 1996; Saxton, Wu & Pongracic 1997; Saxton et al. 1998; Hujeirat & Papaloizou 1998; Saxton & Wu 1999). Many of these shocks are found to be thermally unstable. For instance, a numerical study by Langer et al. (1981) showed that the post-shock accretion flow in magnetic cataclysmic variables (mCVs), binaries in which a magnetic white dwarf accretes material from a red-dwarf companion star, suffers thermal instabilities and hence fails to attain a steady-state. The accretion shock is driven to oscillate, giving rise to quasi-periodic oscillations in the optical luminosity. A similar conclusion was obtained by Chevalier & Imamura (1982), using a linear perturbative analysis.

The stability of the radiative shock depends on the energy transport processes. In the case of accretion shocks in mCVs, thermal bremsstrahlung and cyclotron radiation are the most important cooling processes (e.g. Lamb & Masters 1979; King & Lasota 1979). Bremsstrahlung and cyclotron cooling have very different temperature dependences, and hence influence the stability properties of the accretion shock differently.

In the stability analysis of Chevalier & Imamura (1982), the total cooling effects were approximated by a single radiative loss term $\Lambda \propto \rho^a T^b$ depending on temperature T and density ρ . Various choices of the power-law indices (e.g. $a = 0.5$ and $b = 2$ for bremsstrahlung cooling) were investigated, and they have found that radiative shocks with larger b (i.e. stronger temperature dependence) are more stable against perturbations.

The individual cooling processes were subsequently considered explicitly in the numerical study of accretion onto magnetic white dwarfs by Chanmugam et al. (1985). An effective cooling term was constructed to mimic the effects due to optically thick cyclotron cooling. Their study showed that efficient cyclotron cooling stabilises the shock. Wu et al. (1992, 1996) further investigated the same system and found that in spite of the suppression of shock oscillations in the presence of cyclotron cooling, the oscillation frequency appears to increase quadratically with the magnetic-field strength. Moreover, each of the cooling processes, bremsstrahlung and cyclotron, dominates in about half of the phases of an oscillatory cycle, allowing the perpetuation of small-amplitude oscillations provided that the magnetic field is moderate or weak ($B \lesssim 10$ MG).

Linear perturbative analyses of accretion shocks with bremsstrahlung and cyclotron cooling were carried out by Saxton et al. (1997). A composite cooling function (following Wu, Chanmugam & Shaviv 1994) was considered, comprising the sum of a term for bremsstrahlung cooling and an effective term for cyclotron cooling. The analysis was further extended by Saxton et al. (1998), in which the cooling function is a sum of terms for bremsstrahlung cooling ($\Lambda_{\text{br}} \propto \rho^2 T^{0.5}$) and a second power-law process with a destabilizing influence ($\Lambda_2 \propto \rho^a T^b$ for $b \geq 1$). The cases considered included that of a cooling term ($\Lambda_{\text{cy}} \propto \rho^{0.15} T^{2.5}$) effectively approximating the energy loss due to cyclotron radiation in the geometry and flow conditions of the post-shock regions of mCVs. It was found that a simple comparison of cooling and oscillation timescales is insufficient to understand the instabilities of the shock under various modes.

When the radiative cooling is fast compared to the electron-ion energy exchange, the electron and ion temperatures are generally unequal. Imamura et al. (1996) considered bremsstrahlung and Compton cooling, and a more general perturbation of the shock in both longitudinal and transverse directions. Their study showed that the electron-ion exchange process and the presence of transverse perturbations can destabilize each mode compared to the purely longitudinal and one-temperature cases. Saxton & Wu (1999) generalised the works of Chevalier & Imamura (1982), Imamura et al. (1996), Saxton et al. (1997) and Saxton et al. (1998) for radiative accretion shocks by considering multiple cooling processes explicitly, the two-temperature effects and transverse perturbations (as for a corrugated shock). In the case of mCVs the introduction of two-temperature effects complicated and broke down the strictly monotonic stabilisation of modes with increasing cyclotron efficiency in one-temperature shocks with bremsstrahlung and cyclotron cooling, and the influence of transverse perturbation was not always able to destabilize oscillatory modes in the presence of both bremsstrahlung and cyclotron cooling. (For a review of stability of accretion shocks, see Wu 2000.)

The present paper expands upon the studies of the eigenvalue in Saxton & Wu (1999) to examine the amplitudes and phases of the eigenfunctions which describe the response of the post-shock structure to perturbations of the shock position. As an illustrative case we consider the accretion shocks of magnetic white dwarfs. Knowing the response of the hydrodynamic-variable profiles in turn provides information about other characteristics of thermally unstable shocks, such as the responses of post-shock emissions due to the shock oscillations.

2 FORMULATION

2.1 Hydrodynamics

In accretion onto white dwarfs, the supersonic flow meets a stand-off shock where the inwards falling matter is abruptly decelerated to attain a subsonic speed. The shock sits above the white-dwarf surface at a height $x_s \approx \frac{1}{4}v_{\text{ff}} t_{\text{cool}}$, where the free-fall velocity is $v_{\text{ff}} = (2GM_{\text{wd}}/R_{\text{wd}})^{1/2}$, the cooling timescale is $t_{\text{cool}} \sim n_e k_B T_s / \Lambda$, and Λ is a radiative cooling function. (M_{wd} and R_{wd} are the white-dwarf mass and radius respectively; k_B is the Boltzman constant; n_e is the electron number density; and T_s is the shock temperature.)

The time-dependent mass continuity, momentum and energy equations for the post-shock accretion flow are

$$\left(\frac{\partial}{\partial t} + \mathbf{v} \cdot \nabla \right) \rho + \rho (\nabla \cdot \mathbf{v}) = 0, \quad (1)$$

$$\rho \left(\frac{\partial}{\partial t} + \mathbf{v} \cdot \nabla \right) \mathbf{v} + \nabla P = 0, \quad (2)$$

$$\left(\frac{\partial}{\partial t} + \mathbf{v} \cdot \nabla \right) P - \gamma \frac{P}{\rho} \left(\frac{\partial}{\partial t} + \mathbf{v} \cdot \nabla \right) \rho = -(\gamma - 1)\Lambda, \quad (3)$$

$$\left(\frac{\partial}{\partial t} + \mathbf{v} \cdot \nabla \right) P_e - \gamma \frac{P_e}{\rho} \left(\frac{\partial}{\partial t} + \mathbf{v} \cdot \nabla \right) \rho = (\gamma - 1)(\Gamma - \Lambda), \quad (4)$$

where the total radiative cooling function Λ and the electron-ion energy exchange term Γ are local functions of the density ρ , total pressure P , the electron partial pressure P_e , and the flow velocity \mathbf{v} . The explicit form of the exchange function is

$$\Gamma = \frac{4\sqrt{2\pi}e^4 n_e n_i \ln C}{m_e c} \left[\frac{\theta_i - (m_e/m_i)\theta_e}{(\theta_e + \theta_i)^{3/2}} \right], \quad (5)$$

where $n_{i,e}$ are the ion and electron number density, and $\theta_{i,e} = k_B T_{i,e}/m_{i,e}c^2$ with $T_{i,e}$ being the corresponding temperatures. The constants $m_{i,e}$ are the ion and electron masses, e is the electron charge, c is the speed of light and $\ln C$ is the Coulomb logarithm (as in e.g. Melrose 1986). An adiabatic index $\gamma = 5/3$ for an ideal gas is assumed, and the equation of state $P = \rho k_B T / \mu m_H$ is considered, where m_H is the mass of hydrogen atom.

The total cooling function is written in a form of the bremsstrahlung-cooling term and a multiplicative term expressing the ratio of the losses due to the second cooling process and bremsstrahlung cooling. The second process is characterised by its power-law indices of density and electron pressure ($\alpha = b - 1/2$ and $\beta = 3/2 - a + b$ for a general cooling term $\Lambda_2 \propto \rho^a T^b$), and by the parameter ϵ_s , which is the relative efficiency evaluated at the shock. (Larger ϵ_s implies a more efficient second process.)

$$\Lambda \equiv \Lambda_{\text{br}} + \Lambda_2 = \Lambda_{\text{br}} [1 + \epsilon_s f(\tau_0, \pi_e)] , \quad (6)$$

and a function is defined to relate the primary and secondary cooling processes:

$$f(\tau_0, \pi_e) \equiv \frac{4^{\alpha+\beta}}{3^\alpha} \left(\frac{1 + \sigma_s}{\sigma_s} \right)^\alpha \pi_e^\alpha \tau_0^\beta = \left(\frac{P_e}{P_{e,s}} \right)^\alpha \left(\frac{\rho}{\rho_s} \right)^{-\beta} , \quad (7)$$

where $P_{e,s}$ and ρ_s are the shock values of electron pressure and density. The dimensionless parameter $\sigma_s \equiv (P_e/P_i)_s$ is the ratio of electron and ion pressures at the shock. The bremsstrahlung cooling term $\Lambda_{\text{br}} = \mathcal{C} \rho^2 (P_e/\rho)^{1/2}$, where the constant is $\mathcal{C} = (2\pi k_B/3m_e)^{1/2} (2^5 \pi e^6 / 3h m_e c^3) (\mu/k_B m_p^3)^{1/2} g_B$, with m_p the proton mass, h the Planck constant, μ the mean molecular weight and $g_B \approx 1$ the Gaunt factor (see Rybicki & Lightman 1979). For completely ionised hydrogen plasma $\mu = 0.5$ and the constant has a value $\mathcal{C} \approx 3.9 \times 10^{16}$ in c.g.s. units.

2.2 Perturbation

A first-order perturbation is considered for the shock position x_s and velocity v_s :

$$v_s = v_{s1} e^{iky + \omega t} , \quad (8)$$

$$x_s = x_{s0} + x_{s1} e^{iky + \omega t} , \quad (9)$$

where ω is the frequency, and k is the transverse wavenumber of perturbation in the y (transverse) direction. The shock is at rest in the stationary solution, $v_{s0} = 0$, and the perturbed motion of the shock has $v_{s1} = x_{s1}\omega$. The dimensionless frequency and transverse wavenumber are

$$\kappa = x_{s0}k , \quad (10)$$

$$\delta = \frac{x_{s0}}{v_{ff}}\omega . \quad (11)$$

The eigenfrequencies are complex, $\delta = \delta_R + i\delta_I$, with δ_I being the dimensionless frequencies of the oscillations, and δ_R the stability term. When δ_R is positive the perturbation grows; when δ_R is negative the perturbation is damped.

The post-shock position coordinate is labelled by $\xi \equiv x/x_s$, which is $\xi = 1$ at the shock and $\xi = 0$ at the white-dwarf surface. The size of the perturbation is parameterised by $\varepsilon \equiv v_{s1}/v_{ff} = \delta x_{s1}/x_{s0}$. The other scales to be eliminated are x_{s0} the stationary-state shock height and ρ_a the mass density of the pre-shock accretion flow. The hydrodynamic variables are expressed as

$$\rho(\xi, y, t) = \rho_a \cdot \zeta_0(\xi) (1 + \varepsilon \lambda_\zeta(\xi) e^{iky + \omega t}) , \quad (12)$$

$$\mathbf{v}(\xi, y, t) = -v_{ff} \cdot \tau_0(\xi) ((1 + \varepsilon \lambda_\tau(\xi) e^{iky + \omega t}), \varepsilon \lambda_y(\xi) e^{iky + \omega t}) , \quad (13)$$

$$P(\xi, y, t) = \rho_a v_{ff}^2 \cdot \pi_0(\xi) (1 + \varepsilon \lambda_\pi(\xi) e^{iky + \omega t}) , \quad (14)$$

$$P_e(\xi, y, t) = \rho_a v_{ff}^2 \cdot \pi_e(\xi) (1 + \varepsilon \lambda_e(\xi) e^{iky + \omega t}) . \quad (15)$$

where ζ_0 , τ_0 , π_0 and π_e are dimensionless density, velocity, total pressure and electron pressure in the stationary solution; and λ_ζ , λ_τ , λ_y , λ_π and λ_e are complex functions representing the response of the downstream structure to perturbation of the shock height. These five functions describe perturbations of the density, longitudinal velocity, transverse velocity the total pressure and the electron pressure respectively.

Separating the time-independent terms from the hydrodynamic equations yields two algebraic equations and two differential equations for the stationary case:

$$\zeta_0 = 1/\tau_0 , \quad (16)$$

$$\pi_0 = 1 - \tau_0 , \quad (17)$$

$$\frac{d\xi}{d\tau_0} = \frac{\gamma\pi_0 - \tau_0}{\tilde{\Lambda}} , \quad (18)$$

$$\frac{d\pi_e}{d\tau_0} = \frac{1}{\tau_0} \left[\left(1 - \frac{\tilde{\Gamma}}{\tilde{\Lambda}} \right) (\gamma\pi_0 - \tau_0) - \gamma\pi_e \right] . \quad (19)$$

The electron-ion energy exchange and cooling processes are described by appropriate dimensionless forms:

$$\tilde{\Gamma} = (\gamma - 1) (\rho_a v_{ff}^3 / x_{s0})^{-1} \Gamma = (\gamma - 1) \psi_c \psi_{ei} \frac{1 - \tau_0 - 2\pi_e}{\sqrt{\tau_0^5 \pi_e^3}} , \quad (20)$$

$$\tilde{\Lambda} = (\gamma - 1)(\rho_a v_{ff}^3 / x_{s0})^{-1} \Lambda = (\gamma - 1)\psi_c \sqrt{\frac{\pi_e}{\tau_0^3}} [1 + \epsilon_s f(\tau_0, \pi_e)] , \quad (21)$$

where the constant ψ_c is determined by normalisation of the integrated stationary solution and the parameter ψ_{ei} is a ratio between the electron-ion energy exchange and radiative cooling timescales, as described in Imamura et al. (1996) and Saxton & Wu (1999). The physical values of ψ_c and ψ_{ei} are given in Saxton & Wu (1999) and Saxton (1999).

The first-order perturbation is determined by the matrix differential equation:

$$\frac{d}{d\tau_0} \begin{bmatrix} \lambda_\zeta \\ \lambda_\tau \\ \lambda_y \\ \lambda_\pi \\ \lambda_e \end{bmatrix} = \frac{1}{\tilde{\Lambda}} \begin{bmatrix} 1 & -1 & 0 & 1/\tau_0 & 0 \\ -\gamma\pi_0/\tau_0 & 1 & 0 & -1/\tau_0 & 0 \\ 0 & 0 & -(\gamma\pi_0 - \tau_0)/\tau_0 & 0 & 0 \\ \gamma & -\gamma & 0 & 1/\pi_0 & 0 \\ \gamma & -\gamma & 0 & \gamma/\tau_0 & -(\gamma\pi_0 - \tau_0)/\tau_0\pi_e \end{bmatrix} \begin{bmatrix} F_1 \\ F_2 \\ F_3 \\ F_4 \\ F_5 \end{bmatrix} , \quad (22)$$

where the F functions, which are comprised of terms that do not include derivatives of the λ variables, are given by

$$F_1(\tau_0, \pi_e, \xi) = -\xi(\ln \tau_0)' - \delta\lambda_\zeta + i\kappa\tau_0\lambda_y , \quad (23)$$

$$F_2(\tau_0, \pi_e, \xi) = -(\delta - \tau_0')\lambda_\tau + \xi(\ln \tau_0)' + \tau_0'\lambda_\zeta - \tau_0'(\lambda_\pi - \lambda_\tau) , \quad (24)$$

$$F_3(\tau_0, \pi_e, \xi) = -(\delta - \tau_0')\lambda_y + i\kappa(1 - \tau_0)\lambda_\pi + i\kappa\tau_0'\xi/\delta , \quad (25)$$

$$F_4(\tau_0, \pi_e, \xi) = -\pi_0\delta(\lambda_\pi - \gamma\lambda_\zeta) - \tilde{\Lambda} \left[\frac{3}{2}g_2(\tau_0, \pi_e)\lambda_\zeta + \frac{1}{2}g_1(\tau_0, \pi_e)\lambda_e - \lambda_\tau - \lambda_\pi + \frac{1}{\delta} - \frac{\xi}{\tau_0} \right] , \quad (26)$$

$$F_5(\tau_0, \pi_e, \xi) = -\pi_e\delta(\lambda_e - \gamma\lambda_\zeta) - \tilde{\Lambda} \left[\frac{3}{2}g_2(\tau_0, \pi_e)\lambda_\zeta + \frac{1}{2}g_1(\tau_0, \pi_e)\lambda_e - \lambda_\tau - \lambda_e + \frac{1}{\delta} - \frac{\xi}{\tau_0} \right] + \tilde{\Gamma} \left[\frac{5}{2}\lambda_\zeta - \frac{3}{2}\lambda_e + \frac{\pi_0\lambda_\pi - 2\pi_e\lambda_e}{\pi_0 - 2\pi_e} - \lambda_\tau - \lambda_e + \frac{1}{\delta} - \frac{\xi}{\tau_0} \right] , \quad (27)$$

where the primed quantities are derivatives in terms of ξ . The functions $g_1(\tau_0, \pi_e)$ and $g_2(\tau_0, \pi_e)$ are defined as

$$g_1(\tau_0, \pi_e) = 1 + \frac{2\epsilon_s\alpha f(\tau_0, \pi_e)}{1 + \epsilon_s f(\tau_0, \pi_e)} , \quad (28)$$

$$g_2(\tau_0, \pi_e) = 1 - \frac{2}{3} \left[\frac{\epsilon_s\beta f(\tau_0, \pi_e)}{1 + \epsilon_s f(\tau_0, \pi_e)} \right] . \quad (29)$$

The complex matrix differential equation (22) can be decomposed into ten first-order real differential equations in terms of the functions of the stationary solution $\xi(\tau_0)$ and $\pi_e(\tau_0)$, and the real and imaginary parts of each of the perturbed variables. It can be shown that equation (22) is the general description and that the more restricted formulations in Chevalier & Imamura (1982), Saxton et al. (1997, 1998) can be recovered from it under specific assumptions (Appendix A).

2.3 Cooling functions

Optically-thick cyclotron cooling depends not only on the local properties of the hydrodynamic variables but also on the radiation field. A self-consistent description of cyclotron loss usually requires solving the equations for radiative transfer and the hydrodynamics simultaneously. The particular geometry and physical conditions of the magnetically channelled accretion flow in mCVs, however, permit a simplification (see e.g. Cropper et al. 1999). A functional fit involving the density and temperature dependences of the cut-off frequency yields an approximate cooling term $\Lambda_{cy} \propto \rho^{0.15} T_e^{2.5}$ (see Langer et al. 1982; Wu et al. 1994).

In our analysis the effective cyclotron cooling term has power-law indices $(\alpha, \beta) = (2.0, 3.85)$, and the efficiency parameter ϵ_s (Wu 1994) depends upon the temperature, density, magnetic field, and geometry of the emission region. In the limit of a one-temperature accretion flow the efficiency of electron-ion energy exchange ψ_{ei} is large, and the ratio of pressures σ_s tends to unity. For two-temperature shocks, σ_s is determined by the electrons carrying energy into the region above the ion shock, which is a complication beyond the scope of this paper. Following Imamura et al. (1996) and Saxton & Wu (1999), we treat σ_s as a parameter.

2.4 Stationary structure

We assume the stationary-wall condition, which requires a zero terminal velocity at the lower boundary. The stationary solution can be obtained by direct integration, after substituting equations (16) and (17) into equations (18) and (19). In Figure 1 we show the stationary velocity structures (τ_0) of the post-shock region for various choices of the system parameters. The electron and ion sound speeds (c_e, c_i) are also plotted on the same scale. The density is related to the velocity by $\rho_0 = \rho_a/\tau_0$ and the respective temperatures are proportional to the squared sound speeds. Two-temperature effects are more significant in cases when cyclotron cooling is efficient (e.g. $\epsilon_s = 100$), and when the electron-ion exchange is inefficient (i.e. small ψ_{ei}). When two-temperature effects are unimportant, we recover the velocity, density and temperature structure of the one-temperature calculations (Wu 1994; Chevalier & Imamura 1982). A detailed discussion on the two-temperature stationary structures of the post-shock flows and their emission will be presented elsewhere (Saxton, Wu & Cropper, in preparation).

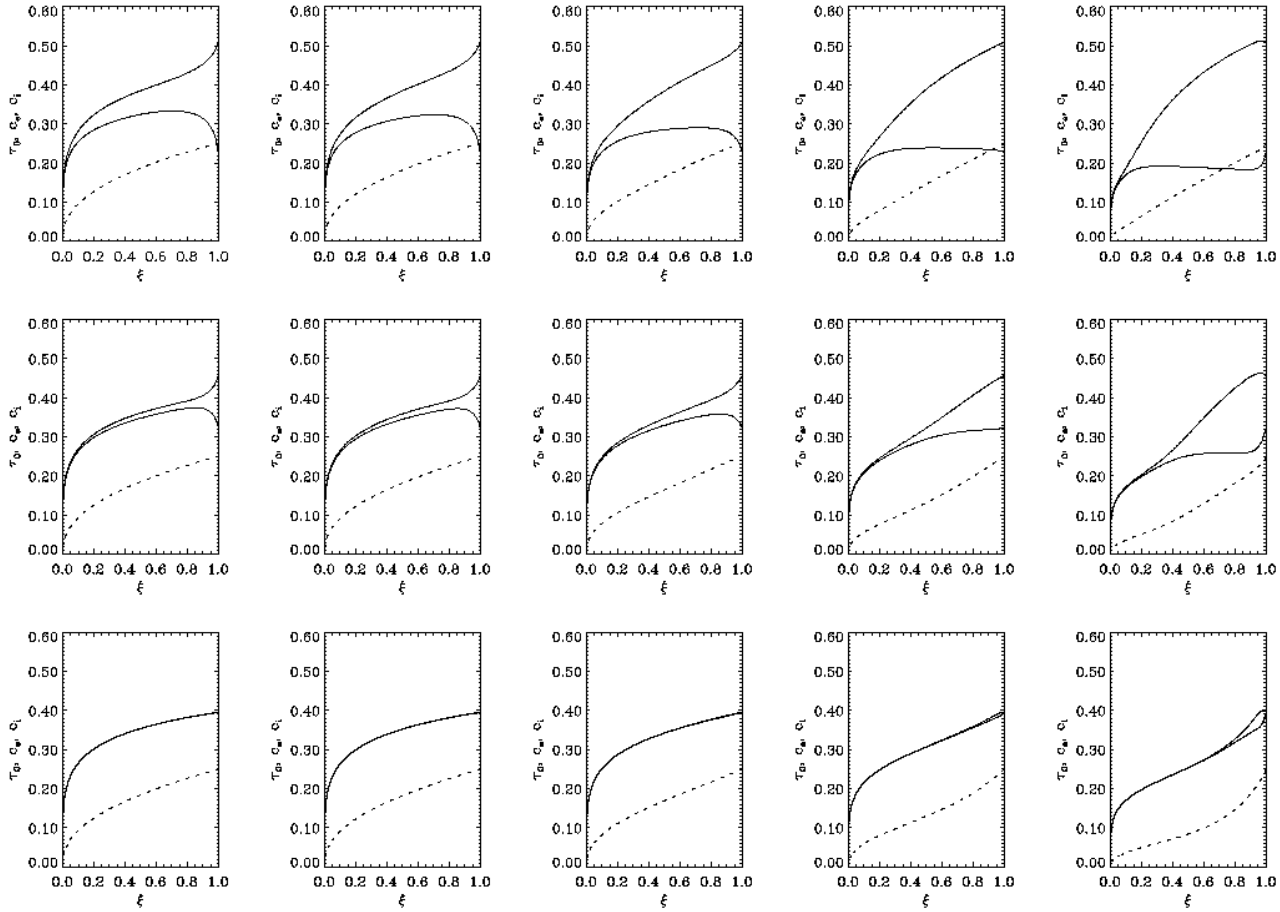


Figure 1. Statinary structures of the post-shock flow, with τ_0 the flow velocity normalised to v_{ff} (dashed lines) as functions of the normalised position ξ . The electron and ion sound speeds are represented by the upper and lower solid curves respectively. The upper, middle and lower rows represent parameter choices $(\sigma_s, \psi_{ei}) = (0.2, 0.1)$, $(\sigma_s, \psi_{ei}) = (0.5, 0.5)$ and, $(\sigma_s, \psi_{ei}) = (1, 10)$ respectively. The columns represent values $\epsilon_s = 0, 0.1, 1, 10, 100$ from left to right.

2.5 Time-dependent solutions

For the time-dependent solution, the set of differential equations for the perturbed variables are integrated numerically from the shock down to the lower boundary for trial values of the complex eigenfrequency δ . The variables at the shock are determined by the shock-jump conditions: $\lambda_\zeta = 0$, $\lambda_\tau = -3$, $\lambda_y = 3i\kappa/\delta$, and $\lambda_\pi = \lambda_e = 2$. The condition at the lower boundary is less well defined. The stationary-wall condition only requires a zero terminal velocity at the bottom for the stationary solution. A lower boundary condition for the perturbed variables, such as the requirement that the flow should stagnate ($\lambda_\tau = 0$), the total pressure be constant ($\lambda_\pi = 0$), or some other condition relating density, pressure and longitudinal velocity (e.g. $\lambda_\zeta + \lambda_\tau = 0$), may be chosen.

The time-dependent solution can be expressed as a linear combination of oscillations of different eigenmodes. For a hydrodynamic variable X , we have

$$X(\xi, t) = X_0(\xi) \sum_n \left[a_n \lambda_{x,n}(\xi) \exp\left(\frac{v_{\text{ff}}}{x_{s0}} \delta_n t\right) \right], \quad (30)$$

where $X_0(\xi)$ is the stationary solution, a_n is the relative strength of the mode n , δ_n the eigenfrequency and $\lambda_{x,n}$ the eigenfunction. While the complex- δ eigenvalues provide information about the global stability properties and oscillating frequencies of the modes, the λ -eigenfunctions describe the more local dynamical properties. The absolute value of the λ -function determines the local oscillation amplitude of the mode, and the phase indicates whether the oscillation of the hydrodynamic variables lags or leads in one region with respect to another.

3 EIGENVALUES

The eigenvalues for two-temperature oscillating shocks with a “perfect” stationary-wall lower boundary condition, i.e. $\tau = \lambda_\tau = 0$ (see Saxton 2001), have been discussed in our previous paper (Saxton & Wu 1999, see also Imamura et al. 1996). More restricted studies on the one-temperature radiative shocks were presented in Saxton et al. (1997) and Saxton & Wu (1998) (see also Chevalier & Imamura 1982). Particular results of these studies include

- (i) In the one-temperature case, the frequencies are quantised like modes of a pipe open at one end, $\delta_l \approx \delta_{IO}(n - 1/2) + \delta_C$ with a small correction δ_C . When two-temperature effects are strong the “stationary-wall” condition at the lower boundary loses importance, and the frequency quantisation becomes more like that of a doubly-open pipe, i.e. $\delta_l \approx \delta_{IO}n$.
- (ii) The frequency spacing δ_{IO} decreases as the efficiency of cyclotron cooling (ϵ_s) increases, but tends to increase when the efficiency of electron-ion energy exchange (ψ_{ei}) decreases.
- (iii) Increasing ϵ_s generally stabilises the modes, but when two-temperature effects are extreme there are situations in which an increase of ϵ_s destabilises some modes.
- (iv) In presence of transverse perturbation, there are maxima of instability at certain values of transverse wavenumber κ for each longitudinal mode. However, there are values of $(\sigma_s, \psi_{ei}, \epsilon_s, \alpha, \beta)$ for which some longitudinal modes are stable at all κ ranges.
- (v) For a given longitudinal mode, the shocks are generally stable against transverse perturbation of sufficiently large κ .
- (vi) Two-temperature effects affect the stability of cyclotron-cooling dominated shocks ($\epsilon_s \gg 1$), but have less influence when bremsstrahlung cooling dominates ($\epsilon_s \approx 0$).

4 EIGENFUNCTIONS

4.1 Amplitude-profile

In one-temperature accretion shocks, the non-trivial eigenfunctions are λ_τ , λ_π , and λ_ζ , corresponding to total pressure, longitudinal velocity and density. In the two-temperature shocks, the non-trivial eigenfunctions also include that of the electron pressure λ_e . When there is a transverse perturbation, a transverse perturbed velocity eigenfunction λ_y becomes important also (see §7).

Our choice of boundary conditions requires that the perturbed longitudinal velocity λ_τ has a fixed value of -3 at the shock, and a stagnant-flow at the white-dwarf surface implies a zero λ_τ at $\xi = 0$. (Here and hereafter in this section, unless specified, the stagnant-flow condition is assumed.) The amplitude profiles generally have local minima and maxima (see Appendix B), which are analogous to the nodes and antinodes in the oscillations of a pipe. The number of nodes and antinodes depend on the harmonic number n , and their positions are determined by the radiative-transport processes and the system geometry. Unlike the nodes of an ideal pipe, the amplitude minima of oscillating shocks do not always go to zero, and the amplitude maxima do not have the same values. Moreover, the nodal features of one hydrodynamic variable may not coincide with those of another hydrodynamic variable.

4.1.1 $|\lambda_\tau|$ -profile

The $|\lambda_\tau|$ profiles do not show very distinctive nodes and antinodes. The amplitude $|\lambda_\tau|$ increases very rapidly with ξ from a zero value at the lower boundary, reaches a plateau or a peak at larger ξ and then declines with a gradual tail towards the shock boundary value. The rapid rise of $|\lambda_\tau|$ occurs only in a small region where $\xi \lesssim 10^{-4}$, and the size of the region seems to be independent of the harmonic number n (see Figure 2). The profiles for $\epsilon_s = 0$ and 1 are similar, with the plateau value of $|\lambda_\tau|$ of the fundamental mode ≈ 3 (e.g. Figure B5). For higher harmonics, the plateau values of $|\lambda_\tau|$ are larger. The maxima (antinodes) generally become more visible when n increases (e.g. Figures B6, B7, B8).

For the cases with large ϵ_s , $|\lambda_\tau|$ has a strong peak near the lower boundary. The peak heights tends to increase with n . It is worth noting that in the extreme of small ψ_{ei} , large σ_s and large ϵ_s (strong two-temperature effects and equal temperature for electrons and ions at the shock), a small peak in $|\lambda_\tau|$ is also present near the shock (see Appendix D.2.4 in Saxton 1999).

4.1.2 $|\lambda_\pi|$ -profile

The boundary value of $|\lambda_\pi|$ is 2 at the shock, but it is not defined at the white-dwarf surface for the stagnant-flow condition. The $|\lambda_\pi|$ profiles do not show distinctive nodes and antinodes for $n = 1$ and 2 . The nodes and antinodes, however, become more visible when n increases and ψ_{ei} becomes small (Figure B7-B10).

4.1.3 $|\lambda_e|$ -profile

The electron pressure eigenfunctions λ_e show nodes and antinodes. The sharpness of the nodes depends on the strength of the electron-ion energy exchange, ψ_{ei} . When the electron-ion energy exchange is efficient, the nodes are weak. When the electron-ion energy exchange is inefficient, (e.g. $\psi_{ei} = 0.1$), the amplitude minima are narrow in ξ and deep in terms of amplitude. (See e.g. the $\epsilon_s = 100$ curves of Figures B1-B4).

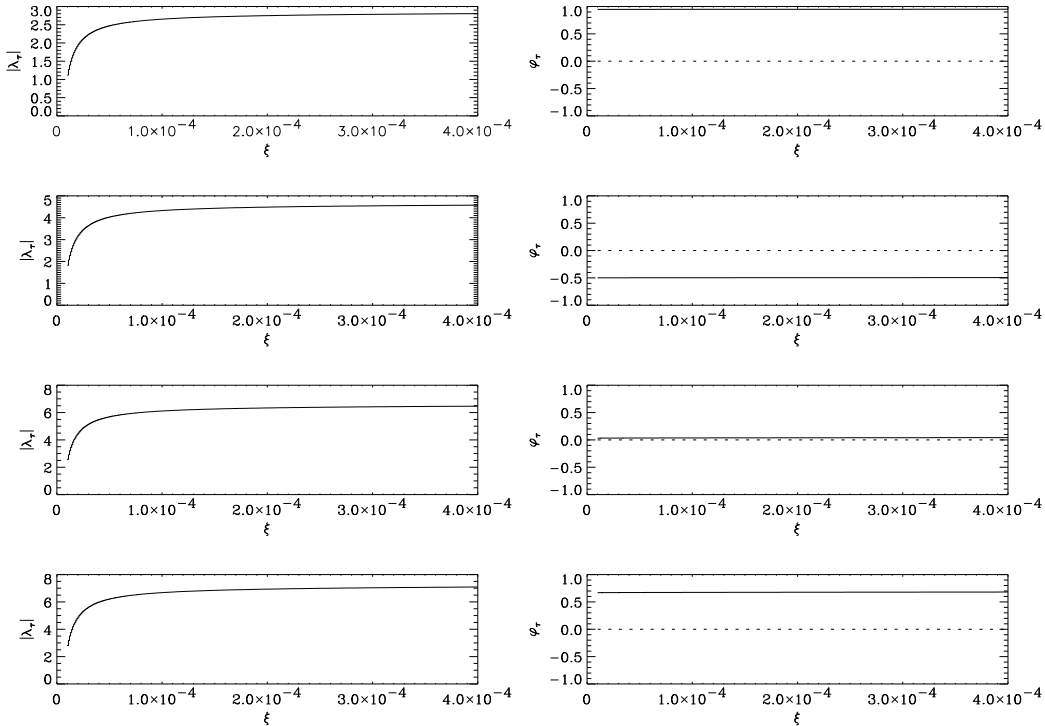


Figure 2. The amplified view $|\lambda_\tau|$ profiles (left column) and the phases φ_τ (right column) near the lower boundary for the case with $(\sigma_s, \psi_{ei}, \epsilon_s) = (0.5, 0.5, 1.0)$ and a stagnant-flow boundary condition ($\lambda_\tau = 0$ at $\xi = 0$). The $|\lambda_\tau|$ profiles and the phases of the modes $n = 1, 2, 3$ and 4 are shown in rows from top to bottom. The $|\lambda_\tau|$ profiles are similar for the four modes, but the phases are very different.

For two-temperature shocks, it is the electron pressure π_e rather than the total pressure π_0 that appears in the cooling terms and electron-ion exchange term. The electron pressure eigenfunction λ_e therefore adopts the role that is played by the total pressure eigenfunction λ_π in the one-temperature case. When the electron-ion energy exchange is weak (i.e. small ψ_{ei}), the λ_π and λ_e eigenfunctions are very different. The different modes have sharp and strikingly different features in $|\lambda_e|$, whereas the total pressure eigenfunction is relatively featureless and smoothly varying. When the energy exchange between electrons and ions is efficient (i.e. large ψ_{ei}), the disparities between their pressures becomes small throughout most of the post-shock region. When the system approaches the one-temperature condition, and the total pressure follows the behaviour of the electron pressure, and the variations of the electron pressure and total pressure eigenfunctions, λ_e and λ_π , are comparable in amplitude over all ξ .

Because of the lower boundary conditions that we assume, the electron and ion temperatures are zero and the electron and ion pressures always become equal at $\xi = 0$. The relative oscillation of the electron pressure must equal the relative oscillation of the total pressure at the lower boundary. I.e. $\lambda_e(\xi) \rightarrow \lambda_\pi(\xi)$ as $\xi \rightarrow 0$. However, there is no condition to determine the particular value at which these quantities must meet at $\xi = 0$, for any given mode under particular conditions.

4.1.4 $|\lambda_\zeta|$ -profile

The density eigenfunctions, λ_ζ , have strong and distinct nodes and antinodes. For each mode the positions and magnitudes of the node-antinode-node sections are affected by the efficiency of cyclotron cooling ϵ_s . When ϵ_s is small ($\lesssim 1$), the nodes are nearly evenly spaced and the antinodes near the shock tend to have lower amplitudes than those nearer to the white-dwarf surface. When ϵ_s is larger, the nodes near the shock are more widely spaced and the antinodes near the shock tend to be higher in amplitude. The innermost antinode in the region $\xi \lesssim 0.1$ becomes higher as ϵ_s increases through the cases of $\epsilon_s = 0, 1, 100$ studied here.

Because of the sharp node and antinode features appearing in the profiles of $|\lambda_\zeta|$ (and $|\lambda_e|$) we suspect that the density and electron pressure may be the quantities which determine the oscillatory properties of the shock. These hydrodynamic variables appear explicitly in the functions for the cooling and electron-ion energy exchange processes. Other hydrodynamic variables (i.e. the flow velocities and the total pressure) have amplitudes varying less rapidly in ξ , probably indicating a less active involvement in determining the oscillatory behaviour of the shock.

For the studied cases of $(\sigma_s, \psi_{ei}, \epsilon_s)$, the modes divide into two classes based on the qualitative features of their amplitude profiles. Profiles of the fundamental and first overtone ($n = 1, 2$) are more alike than the profiles of higher modes. The $n > 2$ modes have $n - 2$ nodes at intermediate ξ positions, whereas the $n = 1, 2$ profiles are slowly-varying in ξ . The actual number

of density nodes in each profile is $n - 1$, including the shock (where $\lambda_\zeta = 0$ as a boundary condition). An additional shallow, and usually indistinct, node occurs near the fixed wall boundary (small ξ) for some cases of large ϵ_s . When two-temperature effects are strong, $|\lambda_e|$ also has sharp nodes for $n > 2$ modes.

4.1.5 nodes, antinodes and sound speeds

The dimensionless electron and ion sound speeds are given by

$$c_e = \sqrt{\gamma \tau_0 \pi_e}, \quad (31)$$

and

$$c_i = \sqrt{\gamma \tau_0 (1 - \tau_0 - \pi_e)} \quad (32)$$

respectively, and the mean sound speed is

$$c_s = \sqrt{\gamma \tau_0 (1 - \tau_0)}. \quad (33)$$

The sound speeds determine the local dynamical time and length scales, which influence the mode spacing. In regions of the post-shock flow where the sound propagation is fast, nodes of the eigenfunctions tend to be further apart.

The sound speeds generally decrease from the shock down to the lower boundary (see Figure 1). When the gradients of the sound speed have less dramatic change (e.g. the case $\epsilon_s = 0$ as in leftmost column of Figure 1) the nodes of the eigenfunctions are more evenly spaced. When ϵ_s is large the sound speeds are proportionately larger in the upper region of the flow, resulting in wider node spacing in the high- ξ region (contrast the different ϵ_s curves of $|\lambda_\zeta|$ in Figure B4).

The local amplitudes of antinodes of the density eigenfunctions are greatest in regions near the shock for large ϵ_s . This is counterintuitive because previous studies (e.g. numerical simulations by Chanmugam et al. 1985, and Wu et al. 1992, 1996) show that oscillations are *globally* suppressed by cyclotron cooling. This global result would lead us to expect lower local amplitudes in the cyclotron-dominated region, and reduced amplitudes in systems with greater ϵ_s . We believe that there is a connection between the increased antinode amplitudes and the increased node spacing in the cyclotron-dominated region when ϵ_s is great. The amplitude enhancement is not related to two-temperature effects, because it occurs in the one-temperature extreme (large ψ_{ei} and $\sigma_s \rightarrow 1$) as well as the general two-temperature cases. The behaviours of the nodes and antinodes (of the density eigenfunction) probably depend more sensitively on the overall form of the stationary solution than on the energy exchange processes present in each region of the flow.

4.2 Phase

The phases of the various perturbed hydrodynamic variables are given the labels φ_ζ , φ_τ , φ_y , φ_π and φ_e for density, longitudinal velocity, transverse velocity, total pressure and electron pressure respectively. The zero values correspond to oscillations in phase with that of the shock height.

4.2.1 Boundary conditions and phase

At the shock ($\xi = 1$) there are boundary conditions on all of the λ variables. The only phase which is not explicitly determined is φ_ζ . Our calculations, however, show that the density oscillation is approximately in quarter-phase ahead of or behind the shock height oscillation, except when $\epsilon_s \sim 100$ (see Figures B2, B6).

There are fewer boundary conditions on the hydrodynamic variables at the bottom of the post-shock region. For the stationary-wall condition, only the longitudinal velocity variable is constrained, $|\lambda_\tau| \rightarrow 0$ as $\xi \rightarrow 0$. The phase φ_τ is not determined. The other perturbed variables have no definite lower boundary values, and their phases depend completely on the energy transport processes.

The phases φ_e and φ_π are not completely independent. Since the electrons and ions have reached the same temperature at the lower boundary, the oscillations of electron pressure and the oscillations of total pressure are identical at $\xi = 0$. The variables λ_π and λ_e have the same values at the shock and the base but different values in between.

4.2.2 Interpretation of $d\varphi/d\xi$

If the phase increases with ξ , we consider the oscillation to be propagating downwards from the shock towards the lower boundary. (This is because the oscillations in the high- ξ region lead the oscillation in the lower- ξ regions.) If the phase decreases with ξ then the oscillation is considered to be propagating upwards. The upward and downward propagation are labelled positive [+] and negative [-] respectively. If a complex λ -function is viewed along the ξ axis, with the real and imaginary λ parts horizontal and vertical, then the complex function appears to wind about the origin in either a clockwise manner for positive propagation, or an anticlockwise manner for negative propagation.

The phase functions can be regarded as having an overall winding between $\xi = 1$ and $\xi = 0$, with local phase glitches. For given $(\sigma_s, \psi_{ei}, \epsilon_s)$, the total winding of each perturbed variable across the interval $0 < \xi < 1$ is a function of harmonic number n . The number of winding cycles is not necessarily an integer. Generally the number of cycles increases with n .

4.2.3 Illustrative cases

For the case of $(\sigma_s, \psi_{ei}) = (0.5, 0.5)$ (see Figures B5-B10), the pressure phases φ_π and φ_e wind positively for the first six modes when $\epsilon_s = 0, 1$. When $\epsilon_s = 100$, φ_e may wind negatively in some regions. For $n = 1$ the winding is negative throughout the entire post-shock region. For $n > 1$ the winding is negative near the lower boundary ($\xi \lesssim 0.05$), but it can be positive or negative elsewhere.

The phase φ_ζ winds in a monotonically negative sense below $\xi \lesssim 0.98$ for the fundamental and first overtone. For the higher harmonics, the winding of φ_ζ undergoes one or more abrupt jumps or reversals in narrow ranges of ξ . There are $n - 2$ phase jumps in φ_ζ , and their positions correspond to the distinct density-amplitude nodes. For the harmonics with $n > 2$, φ_ζ begins with a negative winding near the shock ($\xi = 1$) and remains negatively winding throughout most of the flow, except at the jumps. The jumps can be either positive or negative. Descending from the shock, the first jump is positive, and for many choices of $(\sigma_s, \psi_{ei}, \epsilon_s)$ and n the second jump is negative. The signs of the further jumps depend on the mode and $(\sigma_s, \psi_{ei}, \epsilon_s)$. For $(\sigma_s, \psi_{ei}, \epsilon_s) = (0.5, 0.5, 1)$ the sequence of jumps is $[+, -, -]$ when $n = 5$ ($\epsilon_s = 0, 1$ in Figure B9) and $[+, -, +, -]$ when $n = 6$ ($\epsilon_s = 0, 1$ in Figure B10). In cases where the cyclotron cooling dominates the positive jump in φ_ζ occurs very close to the shock and the subsequent jumps are all negative and indistinct.

4.2.4 Phase “discontinuities”

The sense of a phase jump, e.g. either a modest negative jump in phase or a positive jump by more than half a cycle, is essentially distinct because the phase is seen to either increase or decrease asymptotically on either side of the node discontinuity, i.e. it is determined by the sign of $-d\varphi/d\xi$ in the neighbourhood. In some situations there are critical values of ϵ_s at which the sense of a phase jump changes from positive to negative. For ϵ_s far from the critical values, phase jumps are gradual, being spread relatively broadly in ξ . At the critical ϵ_s the phase jump is a discontinuity without a well-defined sign. Figure 4 shows an example of the changes in structures of a density phase jump with ϵ_s shown near and far from its transition value.

4.2.5 Phases at $\xi = 0$

As not all the phases at the lower boundary are directly constrained by boundary conditions, they can only be obtained by integrating the hydrodynamic equations.

The lower-boundary phase of each perturbed variable increases between a mode n and the consecutive mode $n + 1$, when $(\sigma_s, \psi_{ei}, \epsilon_s)$ is fixed. This inter-mode increment differs slightly between the phases of different hydrodynamic variables. It also depends weakly on harmonic number n . (See Figure 3 for examples of lower-boundary phases for one-temperature systems with different values of the parameter ϵ_s .)

For a particular mode, there are regular phase relationships between different perturbed variables evaluated at the lower boundary. The general trends are as follows: (1) For both one-temperature and two-temperature accretion flows, the density and longitudinal velocity profiles are approximately in phase (i.e. $\varphi_\zeta|_{\xi=0} \approx \varphi_\tau|_{\xi=0}$). (2) The phase φ_π is approximately quarter-phase behind the density and longitudinal velocity phases ($\varphi_\pi|_{\xi=0} \approx \varphi_\zeta|_{\xi=0} - 0.5 \approx \varphi_\tau|_{\xi=0} - 0.5$). The phasings $\varphi_a - \varphi_b$ for two hydrodynamic variables a and b , are approximately constant for $n > 2$. For $n = 1$, and 2 the phasings conform less to the general trend.

5 BOUNDARY CONDITIONS

So far we considered a special case of “stationary wall” in which both τ and λ_τ are zero at $\xi = 0$. We now consider modifications in which the zero-velocity boundary condition for the stationary solution ($\tau_0 = 0$ at $\xi = 0$) is retained but the boundary value of λ_τ is not necessarily zero. For example, the condition $\lambda_\pi = 0$ implies constant (unoscillating) pressure at the lower boundary, whilst allowing oscillations of the velocity at the base of the settling flow. Other interesting conditions studied include $\lambda_\zeta + \lambda_\tau = 0$ (opposite density and velocity oscillations) and $\lambda_\zeta = 0$ (constant density at lower boundary), (see Figure 5). However it is found that the change of boundary conditions has little effect on the frequency sequence δ_1 . The mode stability δ_R only changes appreciably in the regime of large ϵ_s and high harmonic number n . Some choices with reasonable physical interpretations In general most of the choices that we consider yield eigenvalues that are very close to those of the conventional case ($\lambda_\tau = 0$) at $\xi = 0$. Detailed discussions of the effects of boundary conditions on the eigenfunctions can be found in [Saxton \(2001\)](#).

Alternative lower boundary conditions on the stationary variables may be considered in conjunction with alternative conditions on the perturbed variables. However these choices would describe systems that are physically very different from the white-dwarf accretion problem illustrated in this paper. An exploration of the properties of such systems is beyond the scope of this paper, and will be investigated in the future.

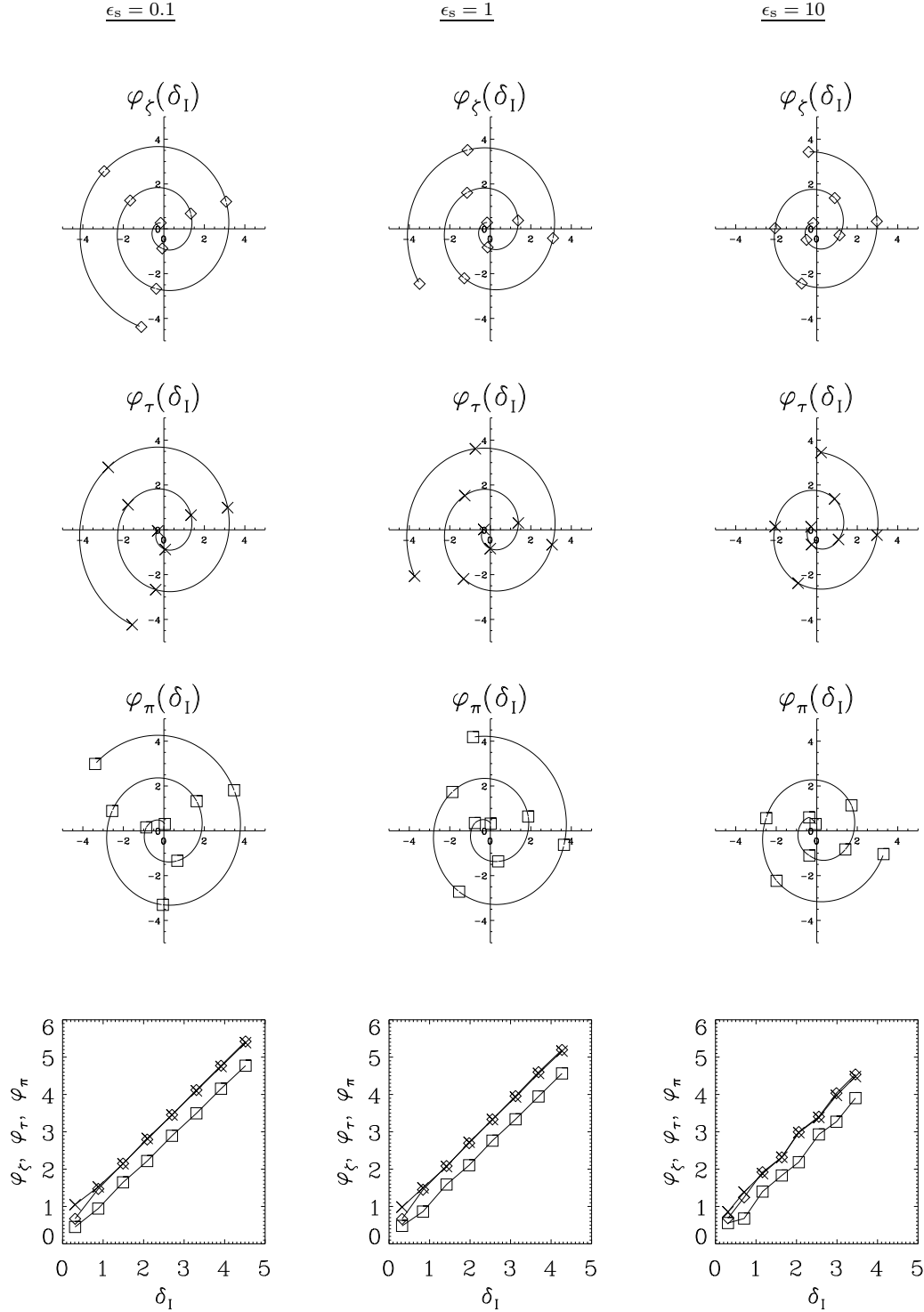


Figure 3. Phase of perturbed variables evaluated at the lower boundary ($\xi = 0$) for the $n = 1, \dots, 8$ modes of one-temperature systems. Phases are defined in relation to the oscillation of shock position. The left, centre and right columns show cases of the efficiency parameter $\epsilon_s = 0.1, 1, 10$ respectively. The polar plots show density, longitudinal velocity and pressure phases as diamonds, crosses and squares. The radius is the oscillatory part of the eigenvalue, δ_I . The bottom row shows equivalent linear plots of phase vs δ_I for the same modes, with the same symbols as the polar plots. The phase variables are defined in terms of π , so that a phase difference $\Delta\varphi = 2$ means a full cycle.

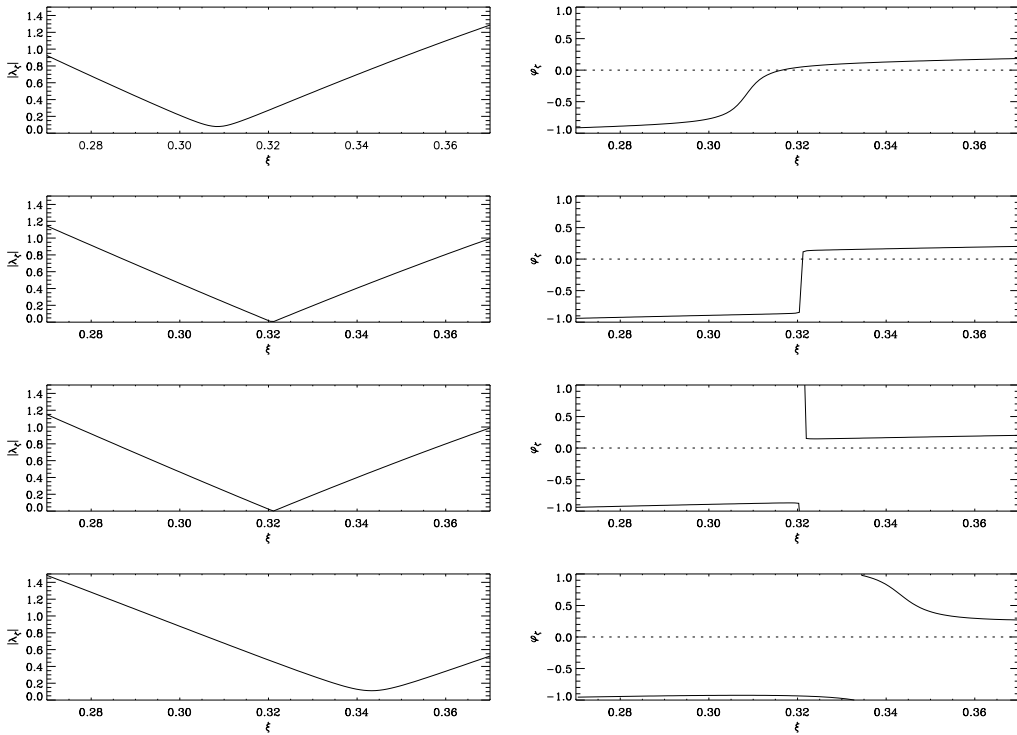


Figure 4. Density eigenfunction of the $n = 3$ eigenmode of a system with $(\sigma_s, \psi_{ei}) = (0.2, 0.1)$, with varying ϵ_s . Far from the critical value for these parameters ($\epsilon_s \approx 6.527$), the phase jumps are broad: first row ($\epsilon_s = 10$); fourth row ($\epsilon_s = 3$). Near the transition, the phase jump is abrupt and the amplitude approaches zero at the node: second row ($\epsilon_s = 6.55$); third row ($\epsilon_s = 6.5$).

6 LUMINOSITY RESPONSE

The total power (normalised to $\rho_a v_{ff}^2$) is given by integrating the cooling function over the whole post-shock structure in the stationary solution:

$$L = \int_0^1 \frac{\tilde{\Lambda}}{\gamma - 1} d\xi = \int_0^{1/4} \frac{[\gamma(1 - \tau_0) - \tau_0]}{\gamma - 1} d\tau_0 = \frac{7\gamma - 1}{32(\gamma - 1)} . \quad (34)$$

For the adiabatic index $\gamma = 5/3$, the total power radiated via all processes is $L = 1/2$, consistent with energy-conservation. The contribution of bremsstrahlung cooling is

$$L_{br,0} = \int_0^{1/4} \frac{[\gamma(1 - \tau_0) - \tau_0]}{\gamma - 1} \frac{1}{1 + \tilde{\Lambda}_{cy}/\tilde{\Lambda}_{br}} d\tau_0 . \quad (35)$$

The second cooling process (which is assumed to be cyclotron cooling) contributes the difference between this value and the total, $L_{cy,0} = L - L_{br,0}$.

It can be shown that the local luminosity responses are described by complex λ -functions that are analogous to the eigenfunctions of the hydrodynamic variables. The bremsstrahlung and cyclotron luminosity response functions, normalised to ϵ , are

$$\lambda_{br} = \frac{3}{2}\lambda_\zeta + \frac{1}{2}\lambda_e \quad (36)$$

and

$$\lambda_{cy} = (0.15 - 2.5)\lambda_\zeta + 2.5\lambda_e \quad (37)$$

for the conditions of accreting magnetic white dwarfs. For a particular mode the λ_{br} and λ_{cy} profiles describe what could be regarded as eigenfunctions of the effect of the oscillations on the cooling emission.

The amplitude and phase profiles of the modes reveal several regularities. The phases φ_{br} and φ_{cy} are both zero at the shock, $\xi = 1$ (see Figures 6-7), meaning that the emission due to both processes locally near the shock oscillates in phase with the oscillation of the shock height. The function $|\lambda_{br}|$ has a minimum in amplitude at or near the shock, and the cyclotron function $|\lambda_{cy}|$ has a maximum in the same vicinity. In between the upper and lower boundaries there is no simple relationship between the phases of the two functions. Near the lower boundary, both eigenfunctions reach their maximum amplitudes for

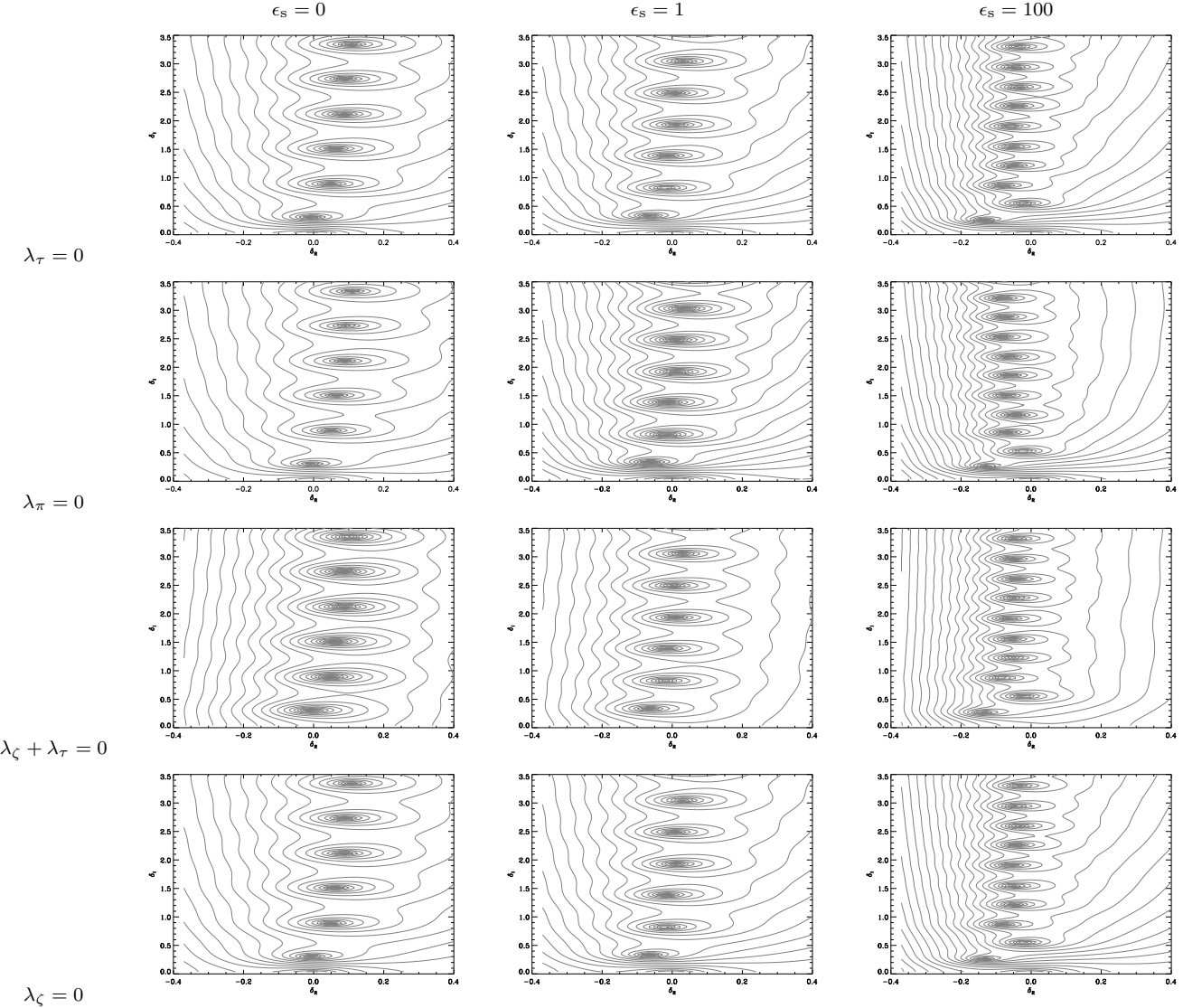


Figure 5. Eigenplanes for $(\sigma_s, \psi_{ei}) = (0.5, 0.5)$ and $\epsilon_s = 0, 1, 100$ with alternative lower boundary conditions. Contours indicate the agreement between integrated values of the perturbed variables at given complex δ and the boundary condition. The top row is for the conventional zero-velocity boundary condition $\lambda_\tau = 0$. The upper-middle row is for $\lambda_\pi = 0$, meaning constant pressure at the lower boundary; the lower-middle row is for $\lambda_\zeta + \lambda_\tau = 0$, which relates to the strict relation $\rho \propto 1/v$; and the bottom row is for $\lambda_\zeta = 0$, which is a condition of constant density at the boundary.

any given mode, and these maxima are higher for modes with higher harmonic number n . At the lower boundary, $\xi = 0$, the oscillations of the two cooling processes are in antiphase. However, in almost all cases the antinodes of λ_{br} occur at the nodes of λ_{cy} and the nodes of λ_{br} occur at the antinodes of λ_{cy} . There is no obvious relation between the luminosity responses λ_{br} , λ_{cy} and the eigenvalues δ .

Multiplying λ_{br} and λ_{cy} by the respective cooling functions and integrating over the entire post-shock region yields the luminosity responses for a small shock-height perturbation ε (see subsection 2.2):

$$L_{br,1} = \varepsilon \int_0^{1/4} \frac{\tilde{\Lambda}_{br}}{\gamma - 1} \lambda_{br} \frac{d\xi}{d\tau_0} d\tau_0 = \varepsilon \int_0^{1/4} \frac{[\gamma(1 - \tau_0) - \tau_0]}{\gamma - 1} \frac{\tilde{\Lambda}_{br}}{\tilde{\Lambda}_{br} + \tilde{\Lambda}_{cy}} \lambda_{br} d\tau_0 , \quad (38)$$

and

$$L_{cy,1} = \varepsilon \int_0^{1/4} \frac{\tilde{\Lambda}_{cy}}{\gamma - 1} \lambda_{cy} \frac{d\xi}{d\tau_0} d\tau_0 = \varepsilon \int_0^{1/4} \frac{[\gamma(1 - \tau_0) - \tau_0]}{\gamma - 1} \frac{\tilde{\Lambda}_{cy}}{\tilde{\Lambda}_{br} + \tilde{\Lambda}_{cy}} \lambda_{cy} d\tau_0 . \quad (39)$$

$L_{br,1}$ is different for different modes, and so is $L_{cy,1}$. Moreover, the modes which have high-amplitude $L_{cy,1}$ oscillations do not necessarily have strong oscillations in $L_{br,1}$.

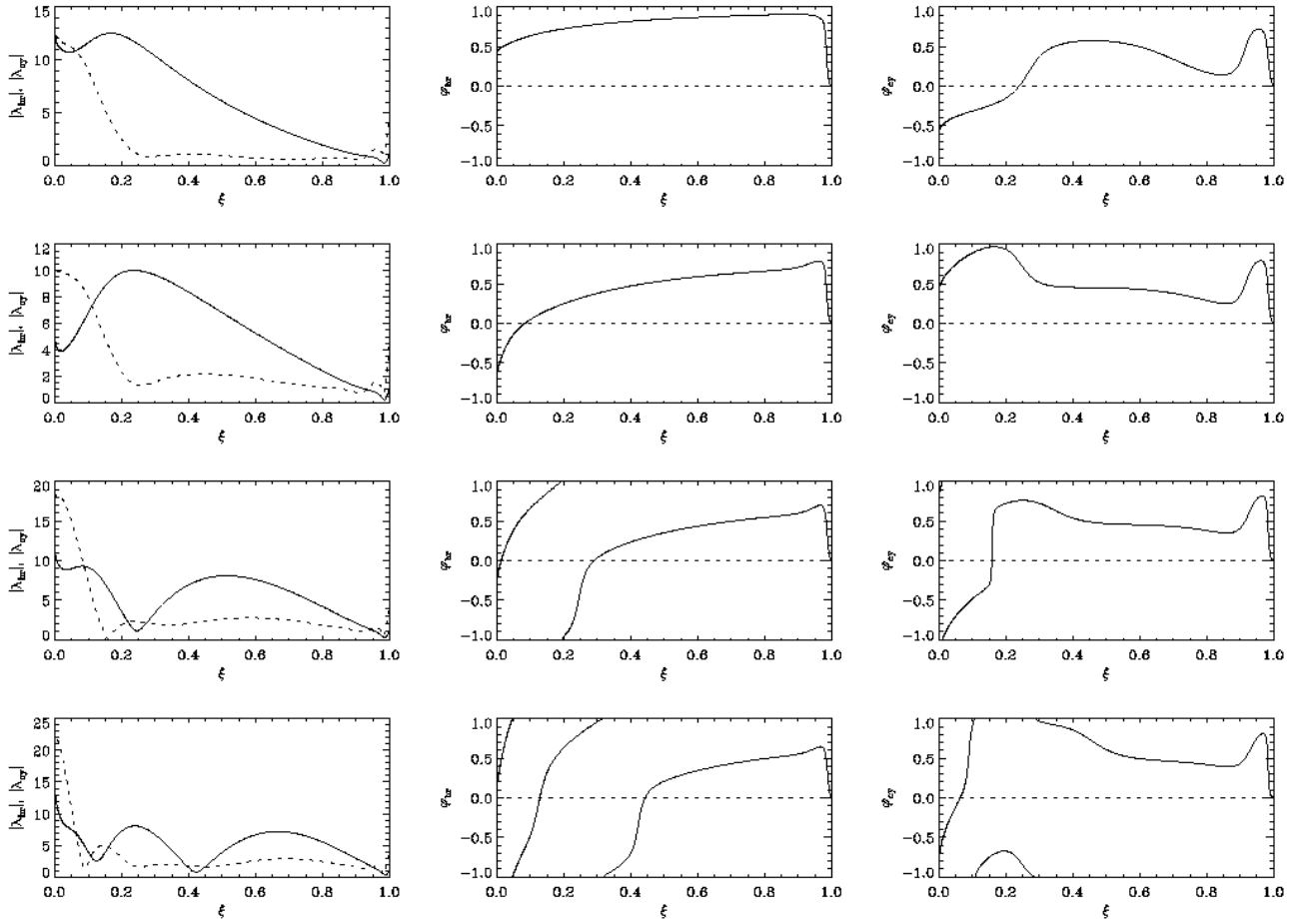


Figure 6. Profiles of luminosity perturbed variables, λ_{br} and λ_{cy} , in modes $n = 1, 2, 3, 4$ from top to bottom. This choice of system parameters, $(\sigma_s, \psi_{ei}, \epsilon_s) = (0.2, 0.1, 100)$, gives strong two-temperature effects and cyclotron cooling dominates the cooling. The left column shows the amplitudes for bremsstrahlung luminosity $|\lambda_{br}|$ (solid line) and cyclotron $|\lambda_{cy}|$ (dotted line). Central and right columns are the phase profiles, φ_{br} and φ_{cy} , with the dotted straight line being a zero-phase reference.

In Table 1 we show the integrated luminosity responses, scaled according to the amplitude of shock-height oscillation ε . These quantities are proportional to the relative variations in bremsstrahlung (cyclotron) emission.

$L_{br,1}$ and $L_{cy,1}$ do not show obvious dependence on δ_R , however they seem to be dependent on the system parameters $(\sigma_s, \psi_{ei}, \epsilon_s)$. Whether or not $|L_{br,1}|/L_{br,0} > |L_{cy,1}|/L_{cy,0}$ depends strongly on ϵ_s , but is only weakly dependent on σ_s and ψ_{ei} .

The complex phases of the values $L_{br,1}$ and $L_{cy,1}$, are $\Phi_{br}(n)$ and $\Phi_{cy}(n)$ respectively for each mode n , are listed in Table 2. Depending on the difference between the phases, the waxing and waning of the emission due to one cooling process may follow or lead the other process, or else they may be in phase or antiphase.

For small ϵ_s and for a given mode n , the phases $\Phi_{br}(n)$ and $\Phi_{cy}(n)$ are nearly constant throughout the (σ_s, ψ_{ei}) parameter space. The two-temperature parameters (σ_s, ψ_{ei}) are almost ineffectual in the small- ϵ_s regime. For constant σ_s and ϵ_s , decreasing ψ_{ei} causes the phase difference $\Phi_{cy}(n) - \Phi_{br}(n)$ to decrease. This means that if cyclotron luminosity lags then its lag increases; else if cyclotron luminosity leads bremsstrahlung luminosity then cyclotron's lead decreases.

In general, $\Phi_{br}(1) \approx 0.35\pi$ to 0.5π and $\Phi_{cy}(1) \approx 0.9\pi$ for the fundamental mode in a wide range of system parameters, i.e. cyclotron emission oscillation almost always lags bremsstrahlung emission by $\approx 0.6\pi$. In the extreme cases in which two-temperature effects are so strong that the fundamental mode becomes unstable, e.g. when $(\sigma_s, \psi_{ei}, \epsilon_s) = (1.0, 0.1, 100)$, this relation breaks down. The phase properties are more complicated for the overtones because of more complicated winding and nodes in the λ -functions (see 4.2.2). Therefore no obvious relationships are found between the stability of a mode, the phases Φ_{br} , Φ_{cy} and their differences.

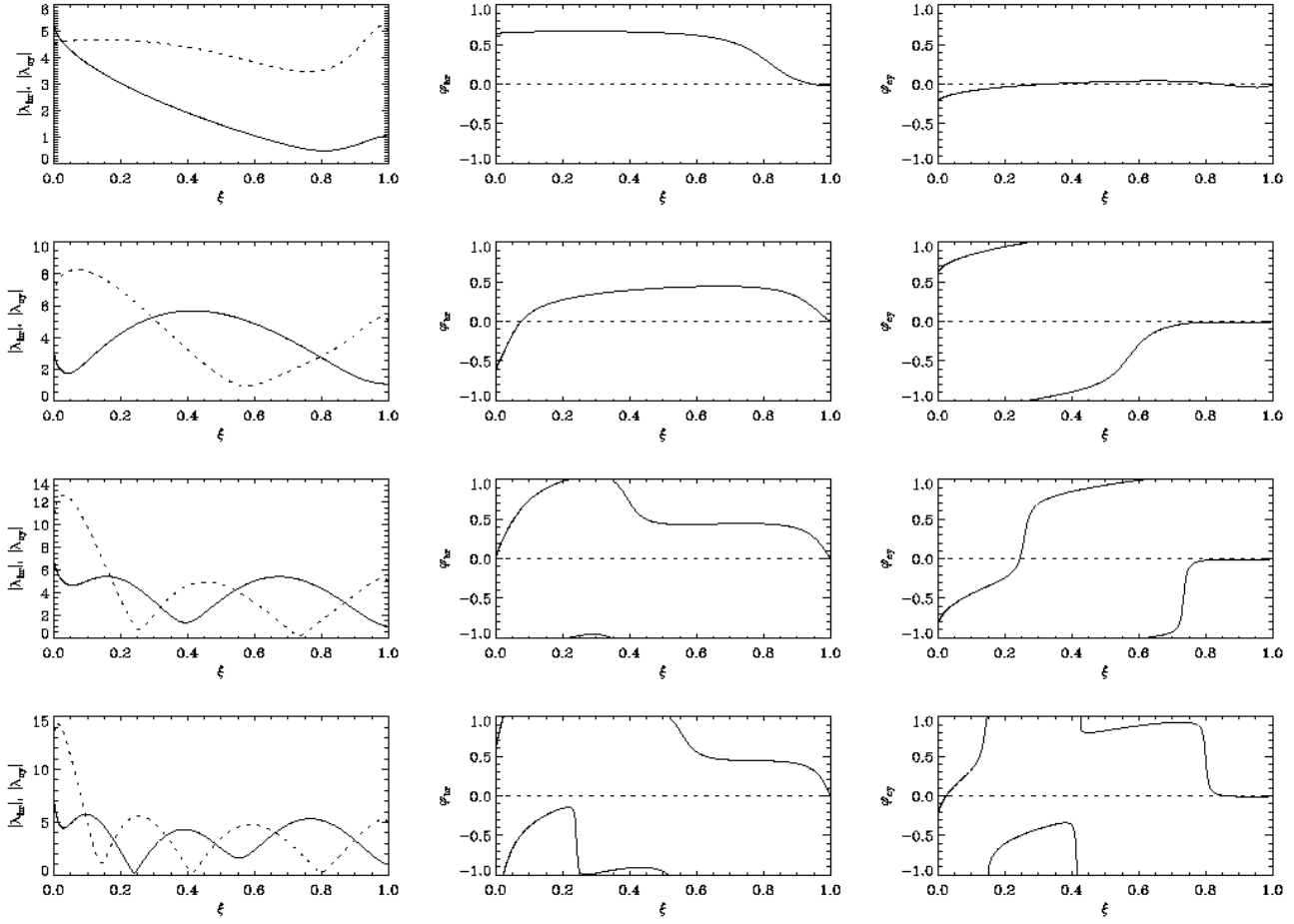


Figure 7. Same as Figure 6 but for $(\sigma_s, \psi_{ei}, \epsilon_s) = (0.5, 0.5, 1)$. This choice of system parameters gives modest two-temperature effects and equal bremsstrahlung- and cyclotron-cooling efficiencies.

7.1 eigen-function profiles

In the absence of transverse perturbations ($\kappa = 0$), the transverse velocity eigenfunction λ_y is zero everywhere. When $\kappa > 0$, the profiles of the other eigenfunctions are modified (see Figures 8, 9). The amplitude $|\lambda_y|$ generally has its maximum value near the lower boundary, and from that value it declines steeply in ξ to the value fixed by the boundary condition at the shock. Increasing κ causes the amplitude $|\lambda_y|$ to increase in the region near the lower boundary, and the slope $d|\lambda_y|/d\xi$ steepens throughout the profile. Greater ϵ_s makes the slope steeper, when κ is fixed. For some κ there are one or more local minima in the $|\lambda_y|$ profile, with the number of minima depending on the harmonic number n .

The transverse velocity phase φ_y generally winds in a negative sense from the shock to the lower boundary (see 4.2.2). The total number of turns of φ_y increases with κ until a threshold is reached. Beyond the threshold there is no winding in φ_y (see Figures 8-9, third panel, right column). The lower boundary values of $|\lambda_\zeta|$, $|\lambda_\tau|$, $|\lambda_\pi|$ and $|\lambda_e|$ all increase with κ beyond the κ -threshold.

The $|\lambda_\zeta|$ and $|\lambda_\tau|$ profiles have the most distinctive features. However the λ_ζ and λ_τ features disappear when κ is sufficiently large. These κ -dependent properties depend on the harmonic number n and the system parameters (e.g. $\kappa \gtrsim 4$ for $(\sigma_s, \psi_{ei}, \epsilon_s) = (0.5, 0.5, 100)$ and $n = 1, 2$, or $\kappa \gtrsim 8$ for $(\sigma_s, \psi_{ei}, \epsilon_s) = (0.5, 0.5, 0)$ and $n = 1, 2$).

The amplitude and phase profiles of the total pressure λ_π and electron pressure λ_e are less dependent upon κ than the density and velocity eigenfunctions are. In the case of $(\sigma_s, \psi_{ei}) = (0.5, 0.5)$ the eigenfunctions for total pressure and electron pressure are not greatly affected by the introduction of a transverse perturbation when κ is small. The total pressure and electron pressure eigenfunctions are much alike because the amplitude and phase profiles match at both the upper and lower boundaries. Increasing κ causes decrease of the lower boundary pressure phase, $\varphi_e|_{\xi=0} = \varphi_\pi|_{\xi=0}$. The phases φ_π and φ_e have similar profiles for small- ϵ_s flows, but the electron pressure develops phase jumps and associated node-like amplitude features when ϵ_s is large. (For a more detailed discussion of the transverse perturbation, see Saxton 1999.)

Table 1. Amplitudes of the oscillations of the total emission in bremsstrahlung and cyclotron radiation, relative to these processes total luminosities in the stationary solution. For each set of the system parameters, the left column indicates whether the mode is stable (–) or unstable (+) in the small-amplitude analysis (see complete eigenvalue results in Saxton & Wu 1999). The middle and right columns are the ε -normalised relative amplitudes $|L_{\text{br},1}|/\varepsilon L_{\text{br},0}$ and $|L_{\text{cy},1}|/\varepsilon L_{\text{cy},0}$ respectively.

σ_s	ψ_{ei}	$\epsilon_s = 0$		$\epsilon_s = 1$		$\epsilon_s = 100$				
		δ_R ?	$ L_{\text{br},1} /\varepsilon L_{\text{br},0}$	$ L_{\text{cy},1} /\varepsilon L_{\text{cy},0}$	δ_R ?	$ L_{\text{br},1} /\varepsilon L_{\text{br},0}$	$ L_{\text{cy},1} /\varepsilon L_{\text{cy},0}$	δ_R ?	$ L_{\text{br},1} /\varepsilon L_{\text{br},0}$	$ L_{\text{cy},1} /\varepsilon L_{\text{cy},0}$
0.2	0.1	–	2.749	*	–	0.924	2.615	–	0.534	0.796
		+	1.650	*	–	0.333	0.736	–	0.203	0.405
		+	2.501	*	–	0.945	0.588	–	0.471	1.156
		+	1.298	*	+	0.859	0.473	–	0.566	0.927
		+	1.685	*	–	1.085	0.375	–	0.544	0.728
		+	2.020	*	+	0.978	0.352	–	0.741	0.594
0.2	0.5	–	2.732	*	–	1.136	3.755	–	1.128	4.057
		+	1.626	*	–	0.213	0.659	–	0.145	0.825
		+	2.493	*	–	1.001	0.202	–	0.471	0.964
		+	1.294	*	–	0.819	0.364	–	0.525	1.093
		+	1.651	*	–	1.107	0.354	–	0.484	0.923
		+	1.977	*	–	0.987	0.329	–	0.688	0.795
0.2	1.0	–	2.732	*	–	1.219	4.227	–	1.244	5.198
		+	1.621	*	–	0.168	1.193	–	0.246	1.072
		+	2.494	*	–	1.054	0.260	–	0.352	0.400
		+	1.291	*	–	0.788	0.099	–	0.550	0.806
		+	1.654	*	–	1.099	0.214	–	0.416	0.924
		+	1.974	*	–	0.998	0.248	–	0.641	0.863
0.5	0.1	+	2.800	*	–	1.277	2.857	–	0.661	0.695
		+	1.628	*	+	0.435	0.727	–	0.279	1.751
		+	2.530	*	+	1.218	0.693	–	0.612	1.494
		+	1.335	*	+	1.096	0.633	+	0.693	1.429
		+	1.652	*	+	1.243	0.557	+	0.860	1.315
		+	2.049	*	+	1.209	0.528	+	0.923	1.215
0.5	0.5	–	2.745	*	–	1.318	4.079	–	1.254	3.600
		+	1.618	*	–	0.345	0.513	–	0.183	0.429
		+	2.497	*	–	1.197	0.190	–	0.715	0.950
		+	1.306	*	+	1.015	0.344	–	0.652	1.173
		+	1.641	*	+	1.228	0.339	–	0.804	1.143
		+	1.983	*	+	1.109	0.331	–	1.102	1.080
0.5	1.0	–	2.739	*	–	1.342	4.453	–	1.425	4.649
		+	1.617	*	–	0.304	0.950	–	0.294	0.898
		+	2.496	*	–	1.215	0.237	–	0.677	0.171
		+	1.297	*	+	0.987	0.199	–	0.666	0.758
		+	1.650	*	–	1.228	0.231	–	0.643	0.929
		+	1.976	*	+	1.091	0.232	–	1.109	0.959
1.0	0.1	+	2.893	*	–	1.635	2.419	+	0.738	0.580
		+	1.601	*	+	0.516	1.024	+	0.350	2.706
		+	2.596	*	+	1.438	1.070	+	0.654	2.588
		+	1.396	*	+	1.278	1.043	+	0.814	2.533
		+	1.591	*	+	1.319	0.975	+	1.192	2.430
		+	2.094	*	+	1.388	0.917	+	1.013	2.311
1.0	0.5	–	2.769	*	–	1.551	4.088	–	1.277	3.048
		+	1.604	*	+	0.415	0.419	+	0.211	0.512
		+	2.505	*	+	1.373	0.284	–	0.806	1.494
		+	1.329	*	+	1.141	0.402	–	0.662	1.737
		+	1.624	*	+	1.303	0.395	–	1.128	1.778
		+	1.998	*	+	1.270	0.402	–	1.202	1.739
1.0	1.0	–	2.752	*	–	1.544	4.516	–	1.441	4.218
		+	1.609	*	+	0.384	0.780	–	0.311	0.462
		+	2.499	*	+	1.374	0.246	–	0.822	0.615
		+	1.309	*	+	1.108	0.251	–	0.672	1.115
		+	1.640	*	+	1.299	0.246	–	0.905	1.319
		+	1.982	*	+	1.245	0.240	–	1.254	1.390

7.2 Luminosity response

Figures 10-11 show the luminosity responses as functions of κ for $n = 1$ and 2. The integrated luminosity amplitudes $|L_{\text{br},1}|$ and $|L_{\text{cy},1}|$ have minima in κ where there are abrupt changes of the phases Φ_{br} and Φ_{cy} respectively. The number of κ -minima is determined by n . For $n = 1$ and $(\sigma_s, \psi_{\text{ei}}) = (0.5, 0.5)$ the $|L_{\text{br},1}|$ minima occur at about $\kappa \sim 1.6, 1.0, 0.6$ for $\epsilon_s = 0, 1, 100$ and the $|L_{\text{cy},1}|$ minima coincide at approximately the same κ -values. For $n = 2$ there are at most two minima of $|L_{\text{br},1}|$. For

Table 2. Total bremsstrahlung and cyclotron emission phases, Φ_{br} and Φ_{cy} , expressed as multiples of π , for the modes $n = 1 \dots 6$ from top to bottom, under given $(\sigma_s, \psi_{\text{ei}}, \epsilon_s)$ conditions. In this convention the phase of the shock-position oscillation is defined as $\Phi_s = 0$. In each set, the third column described the difference between the phases of integrated cyclotron- and bremsstrahlung-luminosity oscillations, $\Phi_{\text{cy}}(n) - \Phi_{\text{br}}(n)$. Negative values indicate the cyclotron luminosity oscillation following the bremsstrahlung luminosity oscillation; and positive values indicate cyclotron luminosity leading bremsstrahlung luminosity.

σ_s	ψ_{ei}	$\epsilon_s = 0$			$\epsilon_s = 1$			$\epsilon_s = 100$		
		$\Phi_{\text{br}} - \Phi_s$	$\Phi_{\text{cy}} - \Phi_s$	$\Phi_{\text{cy}} - \Phi_{\text{br}}$	$\Phi_{\text{br}} - \Phi_s$	$\Phi_{\text{cy}} - \Phi_s$	$\Phi_{\text{cy}} - \Phi_{\text{br}}$	$\Phi_{\text{br}} - \Phi_s$	$\Phi_{\text{cy}} - \Phi_s$	$\Phi_{\text{cy}} - \Phi_{\text{br}}$
0.2	0.1	-0.366	*	*	-0.353	-0.986	-0.663	-0.542	0.928	-0.530
		-0.763	*	*	0.573	-0.336	-0.909	0.388	-0.385	-0.773
		-0.450	*	*	-0.891	-0.319	0.572	0.770	-0.429	0.801
		0.141	*	*	-0.333	-0.263	0.070	-0.855	-0.295	0.560
		0.936	*	*	0.305	-0.280	-0.585	-0.325	-0.271	0.054
		-0.454	*	*	0.892	-0.302	-0.194	0.144	-0.281	-0.425
0.2	0.5	-0.374	*	*	-0.347	-0.989	-0.642	-0.410	0.954	-0.636
		-0.766	*	*	0.517	-0.989	0.494	-0.163	-0.645	-0.482
		-0.458	*	*	-0.957	-0.334	0.623	0.725	-0.367	0.908
		0.116	*	*	-0.441	-0.207	0.234	0.955	-0.373	0.672
		0.913	*	*	0.175	-0.168	-0.343	-0.600	-0.324	0.276
		-0.487	*	*	0.674	-0.170	-0.844	-0.137	-0.265	-0.128
0.2	1.0	-0.376	*	*	-0.339	-0.981	-0.642	-0.340	-0.984	-0.644
		-0.767	*	*	0.396	0.993	0.597	-0.284	-0.827	-0.543
		-0.461	*	*	-0.973	0.934	-0.093	0.810	-0.607	0.583
		0.111	*	*	-0.487	-0.107	0.380	0.879	-0.335	0.786
		0.909	*	*	0.147	-0.050	-0.197	-0.868	-0.324	0.544
		-0.494	*	*	0.612	-0.071	-0.683	-0.244	-0.299	-0.055
0.5	0.1	-0.361	*	*	-0.348	-0.976	-0.628	-0.486	-0.981	-0.495
		-0.762	*	*	0.635	-0.157	-0.792	0.402	-0.231	-0.633
		-0.448	*	*	-0.771	-0.192	0.579	0.775	-0.251	0.974
		0.123	*	*	-0.863	-0.284	0.579	-0.738	-0.192	0.546
		0.931	*	*	0.484	-0.252	-0.736	-0.241	-0.182	0.059
		-0.466	*	*	-0.863	-0.284	0.579	0.219	-0.195	-0.414
0.5	0.5	-0.373	*	*	-0.349	-0.995	-0.646	-0.415	0.976	-0.609
		-0.766	*	*	0.615	0.825	0.210	-0.047	-0.585	-0.538
		-0.458	*	*	-0.820	0.077	0.897	0.743	-0.202	-0.945
		0.112	*	*	-0.240	-0.024	0.216	-0.923	0.270	0.807
		0.911	*	*	0.406	-0.054	-0.460	-0.399	-0.211	0.188
		-0.490	*	*	-0.974	-0.105	0.869	-0.021	-0.189	-0.168
0.5	1.0	-0.375	*	*	-0.347	-0.992	-0.645	-0.359	-0.980	-0.621
		-0.768	*	*	0.593	0.884	0.291	-0.160	-0.878	-0.718
		-0.461	*	*	-0.833	0.660	-0.507	0.782	0.171	-0.611
		0.123	*	*	-0.260	0.235	0.495	0.986	-0.187	0.827
		0.907	*	*	0.388	0.137	-0.251	-0.458	0.193	0.651
		-0.496	*	*	0.996	0.047	-0.949	-0.083	-0.187	-0.104
1.0	0.1	-0.352	*	*	-0.342	-0.889	-0.547	-0.474	-0.299	0.175
		-0.757	*	*	0.700	-0.134	-0.834	0.418	-0.104	-0.522
		-0.444	*	*	-0.690	-0.195	0.495	0.762	-0.146	-0.908
		0.091	*	*	-0.109	-0.243	-0.134	-0.639	0.497	-0.864
		0.924	*	*	0.573	-0.292	-0.865	-0.227	-0.159	0.068
		-0.487	*	*	-0.772	-0.325	0.447	0.251	-0.181	-0.432
1.0	0.5	-0.371	*	*	-0.352	-0.986	-0.634	-0.428	0.994	-0.578
		-0.766	*	*	0.684	0.689	0.005	0.039	-0.067	-0.106
		-0.458	*	*	-0.734	0.113	0.847	0.731	-0.070	-0.801
		0.104	*	*	-0.141	0.008	0.149	-0.814	-0.121	0.693
		0.906	*	*	0.533	-0.047	-0.580	-0.306	-0.137	0.169
		-0.494	*	*	-0.817	-0.111	0.706	0.039	-0.149	-0.188
1.0	1.0	-0.374	*	*	-0.353	-0.991	-0.638	-0.378	-0.975	-0.597
		-0.768	*	*	0.680	0.807	0.127	-0.088	-0.950	-0.862
		-0.461	*	*	-0.743	0.525	-0.732	0.755	0.056	-0.699
		0.105	*	*	-0.151	0.241	0.392	-0.928	-0.063	0.865
		0.904	*	*	0.526	0.160	-0.366	-0.328	-0.093	0.235
		-0.499	*	*	-0.830	0.010	0.840	-0.008	-0.115	-0.107

small ϵ_s the minimum corresponding to a larger κ -value becomes an inflection, e.g. for $\epsilon_s = 0$ the actual amplitude minimum of $|L_{\text{br},1}|$ is at $\kappa \approx 1.8$ and the inflection point is at $\kappa \approx 3.4$.

Both amplitudes, $|L_{\text{br},1}|$ and $|L_{\text{cy},1}|$ are slowly varying in κ when the value of κ is below κ_* , where $\kappa_*(n, \epsilon_s) \approx \frac{1}{2}(2n - 1)\kappa_e(\epsilon_s)$ and κ_e depends on the system parameters. For $(\sigma_s, \psi_{\text{ei}}) = (0.5, 0.5)$, $\kappa_e \sim 1.0$ for $\epsilon_s = 0$. It reduces gradually as the cooling efficiency increases, and $\kappa_e \sim 0.3$ at $\epsilon_s = 100$. For wavenumbers $\kappa > \kappa_*$, both $|L_{\text{br},1}|$ and $|L_{\text{cy},1}|$ increase rapidly with κ . This is a consequence of the increasing amplitudes of the hydrodynamic variables' λ -functions as κ increases. Because bremsstrahlung cooling is most efficient in regions near the lower boundary, $|L_{\text{br},1}|$ tends to rise more steeply with κ than $|L_{\text{cy},1}|$ does.

The integrated luminosity phases Φ_{br} and Φ_{cy} wind with κ . On top of these winding trends, there are phase jumps where the respective $|L_{\text{br},1}|$, $|L_{\text{cy},1}|$ amplitudes reach minima. Away from the minima, both of the phases generally decrease when κ increases. Generally the winding of both phases in κ is more rapid when ϵ_s is large, however for sufficiently large ϵ_s there are modes where Φ_{br} overtakes Φ_{cy} in its variation with κ , e.g. $n = 2$ with $(\sigma_s, \psi_{\text{ei}}, \epsilon_s) = (0.5, 0.5, 100)$. The prevailing winding of the bremsstrahlung phase Φ_{br} is usually more sensitive to κ than the Φ_{cy} is, i.e. $-d\Phi_{\text{br}}/d\kappa$ tends to be greater than $-d\Phi_{\text{cy}}/d\kappa$.

In summary, the presence of transverse perturbations may significantly alter the instability of a mode and modify the luminosity response.

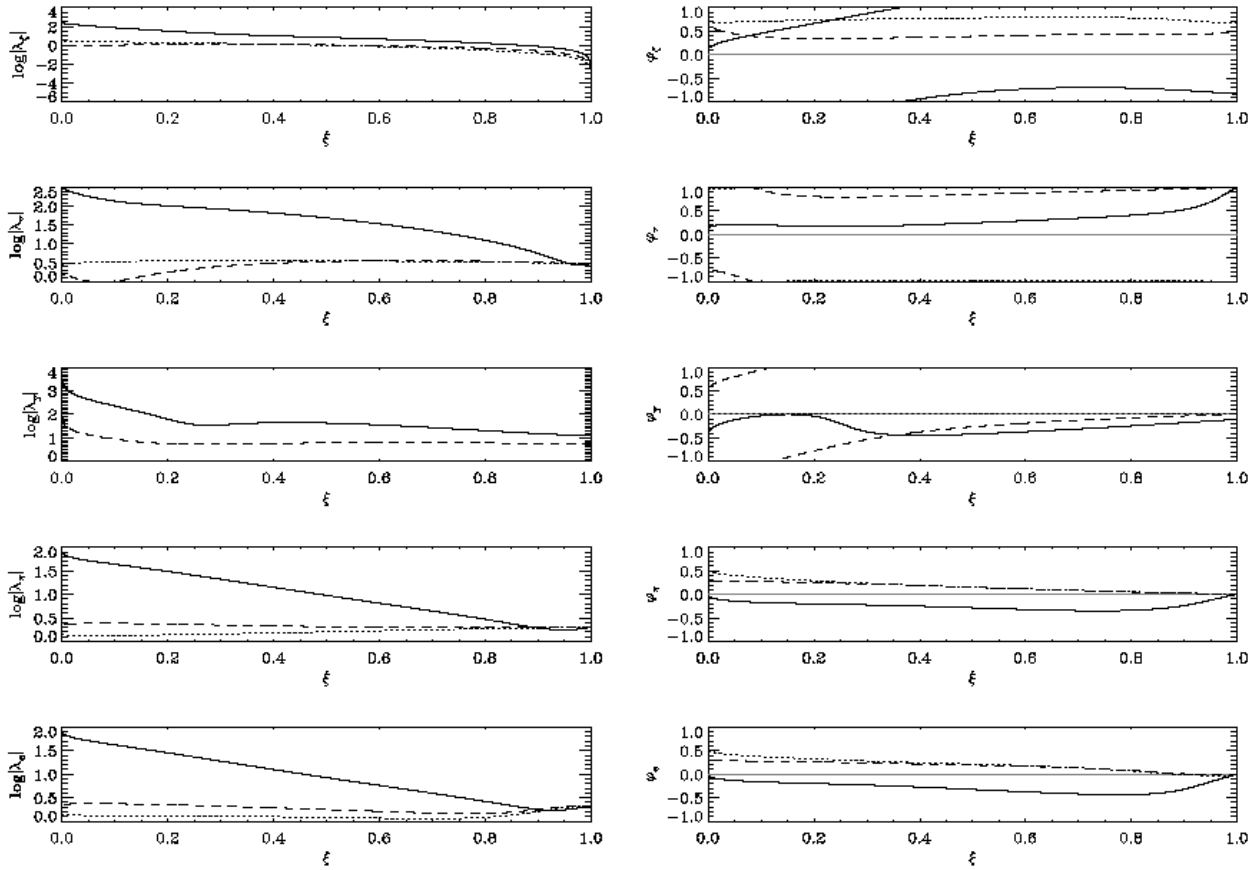


Figure 8. Eigenfunction profiles in the presence of transverse perturbation, for density, longitudinal velocity, transverse velocity, total pressure and electron pressure (from top to bottom), for the $n = 1$ mode with $(\sigma_s, \psi_{ei}, \epsilon_s) = (0.5, 0.5, 1)$. Profiles for wavenumbers $\kappa = 0, 1, 4$ are plotted in dotted, dashed and solid curves respectively. The left column shows logarithms of the amplitudes, and the right column shows the phases. Phases are multiples of π . The dotted line in the phase plots gives reference for zero phase, which is defined to be the phase of the oscillation of shock height (marked in grey).

8 CONCLUSIONS

We have presented a general formulation for the linear analysis of two-temperature radiative shocks with multiple cooling processes. The formulation recovers the restrictive cases in the previous studies such as the one-temperature flows with a single cooling function (Chevalier & Imamura 1982), the one-temperature flows with multiple cooling processes (Saxton et al. 1998) and the two-temperature flows with a single cooling function (Imamura et al 1996). We have applied the formulation to mCVs and investigated the hydrodynamic and emission properties of the time-dependent post-shock accretion flows in these systems. Our findings are summarised as follows.

The amplitude profiles of λ -eigenfunctions show local minima and maxima, which we identify as nodes and antinodes. The nodes and antinodes are prominent only in the eigenfunction profiles of density and electron-pressure. The eigenfunctions for the fundamental and first overtone are more similar to each other than any of the higher overtones. The eigenfunctions for higher-order modes have more nodes.

The phase profiles of the eigenfunctions describing particular hydrodynamic variables circulate about the complex plane as ξ varies from the shock down to the lower boundary. This circulation can be positive or negative overall, or there may be reversals of the winding sense between distinct zones. The abrupt jumps in the phase profiles always coincide with the nodes in the λ -eigenfunction profiles.

The luminosity responses of cyclotron and bremsstrahlung are determined by the λ -eigenfunctions. There is no obvious general relationship between the amplitude or phase luminosity responses and the stability properties of the flow. There are situations in which a mode is unstable but the amplitude of oscillations are larger in the cyclotron luminosity than in the bremsstrahlung luminosity.

For the same stationary condition ($\tau = 0$ at $\xi = 0$), all out choices of perturbed boundary conditions do not show significant differences in the stability properties. We therefore conclude that the stability properties of the flow with stationary-wall boundary is mainly determined by the energy-transport processes.

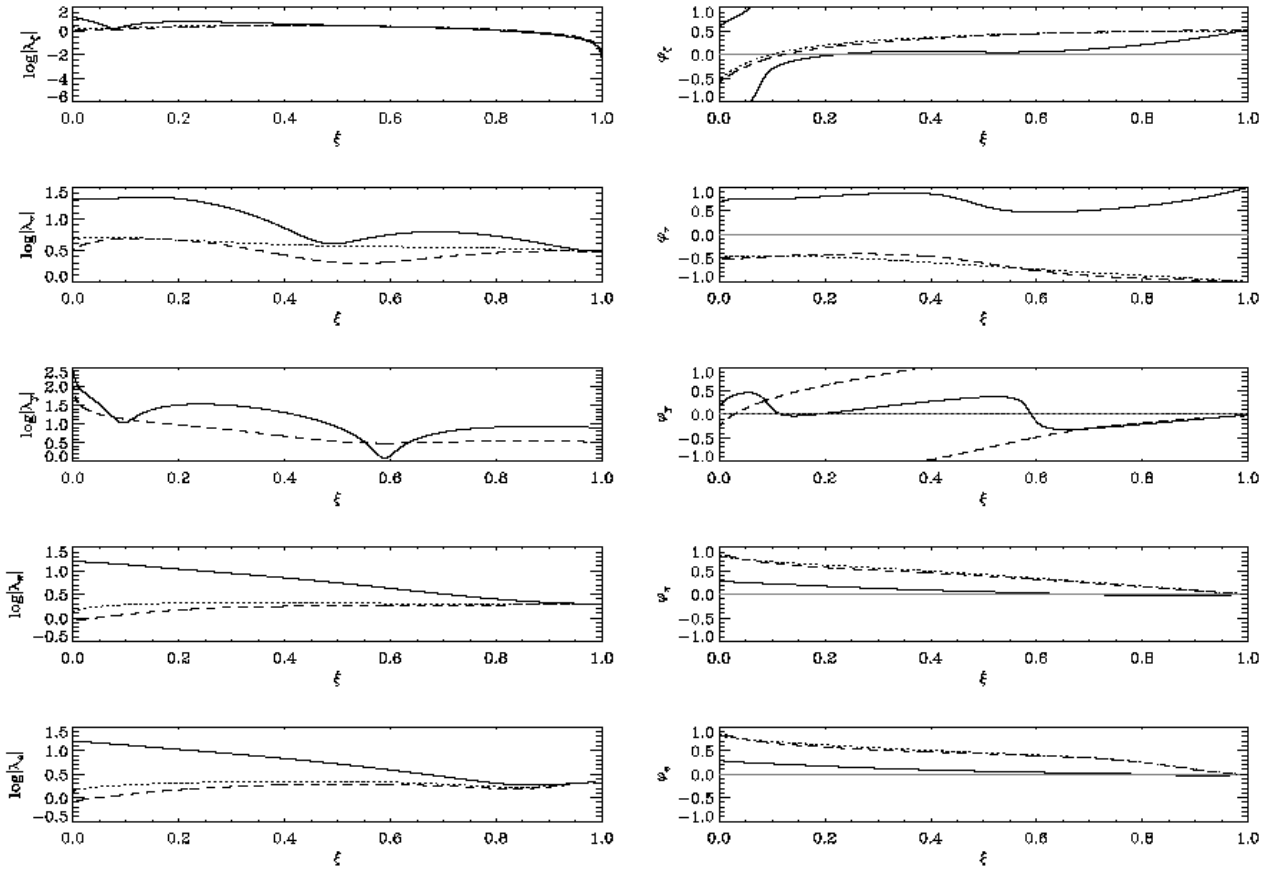


Figure 9. Same as Figure 8 but for $n = 2$.

The presence of a transverse perturbation modifies the eigenfunction profiles of all the hydrodynamic variables. The profiles of electron-pressure and total-pressure eigenfunctions are less affected in comparison with the other eigenfunction profiles. In some range of transverse wavenumber κ , the density and longitudinal-velocity eigenfunction profiles develop extra node features. When κ is large enough ($\lesssim 3$ for $n = 1, 2$), the amplitudes of all eigenfunctions become large near the lower boundary. The amplitudes, however, decrease as the height ξ increases. For some values of the transverse wavenumber ($1 \lesssim \kappa \lesssim 3$), a mode which is stable in the absence of the transverse perturbation can become unstable. However, when κ is very large, the mode is stabilised. The phase difference between the oscillations in the bremsstrahlung and cyclotron luminosity are also modified in the presence of transverse perturbations.

REFERENCES

Aizu, K., 1973. *Prog. Theor. Phys.*, 49, 1184
 Bertschinger, E., 1986, *ApJ*, 304, 154
 Chanmugam G., Langer, S. H., Shaviv, G., 1985, *ApJ*, 299, L87
 Chevalier, R. A., Imamura, J. N., 1982, *ApJ*, 261, 543
 Cropper, M., 1990, *Sp. Sci. Rev.*, 54, 195
 Cropper, M., Wu, K., Ramsay, G., Kocabiyik, A., 1999, *MNRAS*, 306, 684
 Dgani, R., Soker, N., 1994, *ApJ*, 434, 262
 Gaetz, T. J., Edgar, R. J., Chevalier, R. A., 1988, *ApJ*, 329, 927
 Falle, S. A. E. G., 1975, *MNRAS*, 172, 55
 Falle, S. A. E. G., 1981, *MNRAS*, 195, 1011
 Houck, J. C., Chevalier, R. A., 1992, *ApJ*, 395, 592
 Hujeirat, A., & Papaloizou, J. C. B., 1998, *A&A*, 340, 593
 Imamura, J. N., 1985, *ApJ*, 296, 128
 Imamura, J. N., Rashed, H., Wolff, M. T., 1991, *ApJ*, 376, 665
 Imamura, J. N., Wolff, M. T., 1990, *ApJ*, 355, 216
 Imamura, J. N., Wolff, M. T., Durisen, R. H., 1984, *ApJ*, 276, 667
 Imamura, J. N., Aboasha, A., Wolff, M. T., Wood, K. S., 1996, *ApJ*, 458, 327

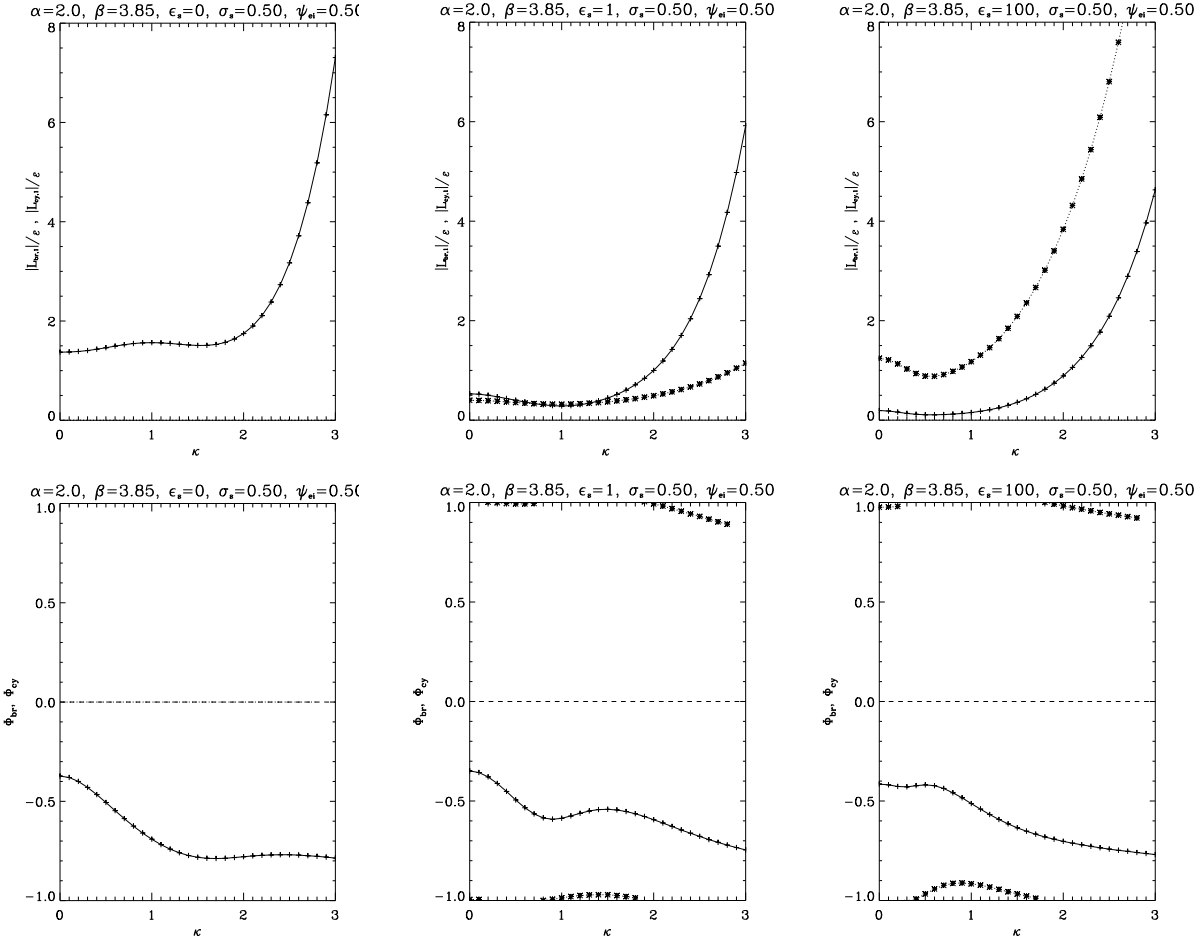


Figure 10. Integrated luminosity response amplitudes and phases for $n = 1$ mode in the presence of transverse perturbations, for the parameters $(\sigma_s, \psi_{ei}) = (0.5, 0.5)$ and $\epsilon_s = 0, 1, 100$ from left to right. The curves corresponding to bremsstrahlung cooling are marked with +; the curves corresponding to cyclotron cooling are marked with \times .

Innes, D. E., Giddings, J. R., Falle, S. A. E. G., 1987a, MNRAS, 224, 179
 Innes, D. E., Giddings, J. R., Falle, S. A. E. G., 1987b, MNRAS, 226, 67
 King, A. R., Lasota, J. P., 1979, MNRAS, 188, 653
 Lamb, D. Q., Masters, A. R., 1979, ApJ, 234, L117
 Langer, S. H., Chanmugam, G., Shaviv, G., 1981, ApJ, 245, L23
 Langer, S. H., Chanmugam, G., Shaviv, G., 1982, ApJ, 258, 289
 Melrose, D. B., 1986, *Instabilities in Laboratory and Space Plasmas*, Cambridge University Press, Cambridge
 Rybicki, G. B., Lightman, A. P., 1979, *Radiative Processes in Astrophysics*, John Wiley & Sons, New York
 Saxton, C. J., 1999, PhD Thesis, University of Sydney, Australia
 Saxton, C. J., 2001, Publ. Astr. Soc. Australia, submitted.
 Saxton, C. J., Wu, K., 1999, MNRAS, 310, 677
 Saxton, C. J., Wu, K., Pongracic, H., 1997, Publ. Astr. Soc. Australia, 14, 164
 Saxton, C. J., Wu, K., Pongracic, H., Shaviv, G., 1998, MNRAS, 299, 862
 Strickland, R., Blodin, J. M., 1995, ApJ, 449, 727
 Tóth, G., Draine, B. T., 1993, ApJ, 413, 176
 Wolff, M. T., Gardner, J., Wood, K. S., 1989, ApJ, 346, 833
 Wu, K., 1994, Proc. Astr. Soc. Australia, 11, 61
 Wu, K., 2000, Space Science Rev., 93, 611
 Wu, K., Chanmugam, G., Shaviv, G., 1992, ApJ, 397, 232
 Wu, K., Chanmugam, G., Shaviv, G., 1994, ApJ, 426, 664
 Wu, K., Pongracic, H., Chanmugam, G., Shaviv, G., 1996, Publ. Astron. Soc. Aust., 13, 93

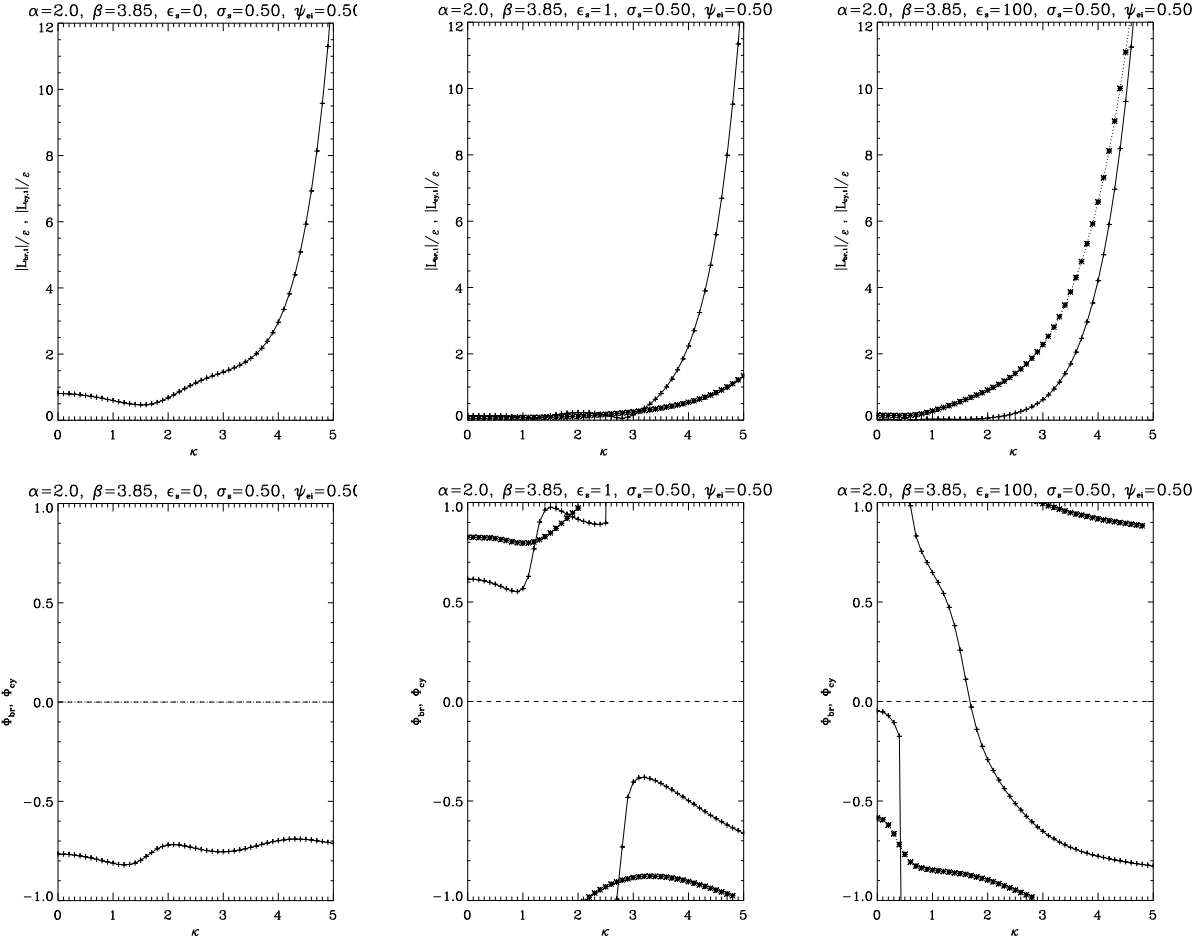


Figure 11. Same as Figure 10 but for the $n = 2$ mode.

APPENDIX A: REDUCTION TO RESTRICTED SYSTEMS

The matrix equation describing the perturbation is

$$\frac{d}{d\tau_0} \begin{bmatrix} \lambda_\zeta \\ \lambda_\tau \\ \lambda_y \\ \lambda_\pi \\ \lambda_e \end{bmatrix} = \frac{1}{\tilde{\Lambda}} \begin{bmatrix} 1 & -1 & 0 & 1/\tau_0 & 0 \\ -\gamma\pi_0/\tau_0 & 1 & 0 & -1/\tau_0 & 0 \\ 0 & 0 & -(\gamma\pi_0 - \tau_0)/\tau_0 & 0 & 0 \\ \gamma & -\gamma & 0 & 1/\pi_0 & 0 \\ \gamma & -\gamma & 0 & \gamma/\tau_0 & -(\gamma\pi_0 - \tau_0)/\tau_0\pi_e \end{bmatrix} \begin{bmatrix} F_1 \\ F_2 \\ F_3 \\ F_4 \\ F_5 \end{bmatrix}. \quad (\text{A1})$$

For systems with a purely longitudinal perturbation, $\kappa = 0$ and the third row and third column of the matrix can be eliminated. The λ_y terms vanish from the remaining F functions, and the equation for λ_y decouples from the rest of the perturbed variables is simply $(\ln \lambda_y)' = \delta/\tau_0 - (\ln \tau_0)'$ or otherwise $\lambda_y' = \lambda_y(\delta - \tau_0')/\tau_0$. The two-temperature system with purely longitudinal perturbations is described by this reduced matrix equation, with corresponding F functions that omit all terms of λ_y :

$$\frac{d}{d\tau_0} \begin{bmatrix} \lambda_\zeta \\ \lambda_\tau \\ \lambda_\pi \\ \lambda_e \end{bmatrix} = \frac{1}{\tilde{\Lambda}} \begin{bmatrix} 1 & -1 & 1/\tau_0 & 0 \\ -\gamma\pi_0/\tau_0 & 1 & -1/\tau_0 & 0 \\ \gamma & -\gamma & 1/\pi_0 & 0 \\ \gamma & -\gamma & \gamma/\tau_0 & -(\gamma\pi_0 - \tau_0)/\tau_0\pi_e \end{bmatrix} \begin{bmatrix} F_1 \\ F_2 \\ F_4 \\ F_5 \end{bmatrix}. \quad (\text{A2})$$

In the single-temperature limit, ψ_{ei} becomes large and the electron and ion pressures both equal half of the total pressure, i.e. we have $2\pi_e \rightarrow \pi_0 = 1 - \tau_0$, and $\lambda_e \rightarrow \lambda_\pi$ throughout the entire post-shock flow. Moreover, $F_5 \rightarrow \frac{1}{2}F_4$. Then we can eliminate the fifth row of (A1), yielding

$$\frac{d}{d\tau_0} \begin{bmatrix} \lambda_\zeta \\ \lambda_\tau \\ \lambda_y \\ \lambda_\pi \end{bmatrix} = \frac{1}{\tilde{\Lambda}} \begin{bmatrix} 1 & -1 & 0 & 1/\tau_0 \\ -\gamma\pi_0/\tau_0 & 1 & 0 & -1/\tau_0 \\ 0 & 0 & -(\gamma\pi_0 - \tau_0)/\tau_0 & 0 \\ \gamma & -\gamma & 0 & 1/\pi_0 \end{bmatrix} \begin{bmatrix} F_1 \\ F_2 \\ F_3 \\ F_4 \end{bmatrix}. \quad (\text{A3})$$

Reducing the system to a one-temperature form with purely longitudinal perturbations leaves only three non-trivial perturbed variables and hence a 3×3 coefficient matrix

$$\frac{d}{d\tau_0} \begin{bmatrix} \lambda_\zeta \\ \lambda_\tau \\ \lambda_\pi \end{bmatrix} = \frac{1}{\tilde{\Lambda}} \begin{bmatrix} 1 & -1 & 1/\tau_0 \\ -\gamma\pi_0/\tau_0 & 1 & -1/\tau_0 \\ \gamma & -\gamma & 1/\pi_0 \end{bmatrix} \begin{bmatrix} F_1 \\ F_2 \\ F_4 \end{bmatrix}, \quad (\text{A4})$$

which is equivalent to that in Saxton et al. (1997) and Saxton et al. (1998).

APPENDIX B: EIGENFUNCTION PROFILES

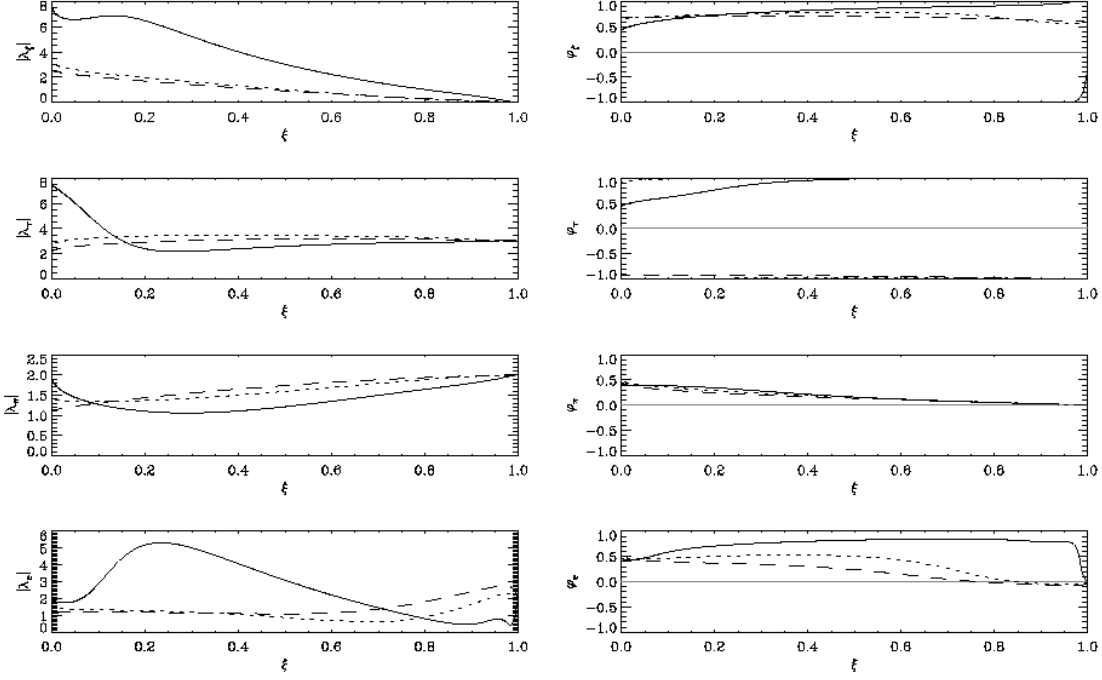


Figure B1. Eigenfunctions for $n = 1$ mode with $(\sigma_s, \psi_{ei}) = (0.2, 0.1)$ and $\epsilon_s = 0, 1, 100$ for dashed, dotted and solid lines respectively. Amplitudes are shown in the left column, phase profiles on the right.

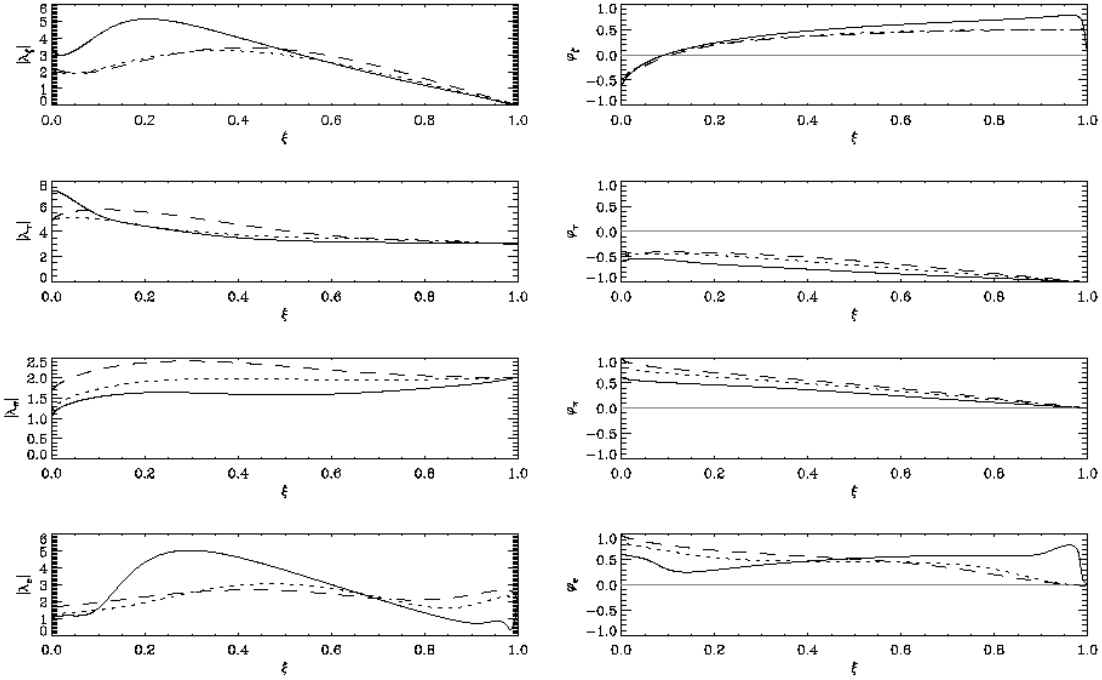


Figure B2. Same as Figure B1 but with $n = 2$ and $(\sigma_s, \psi_{ei}) = (0.2, 0.1)$.

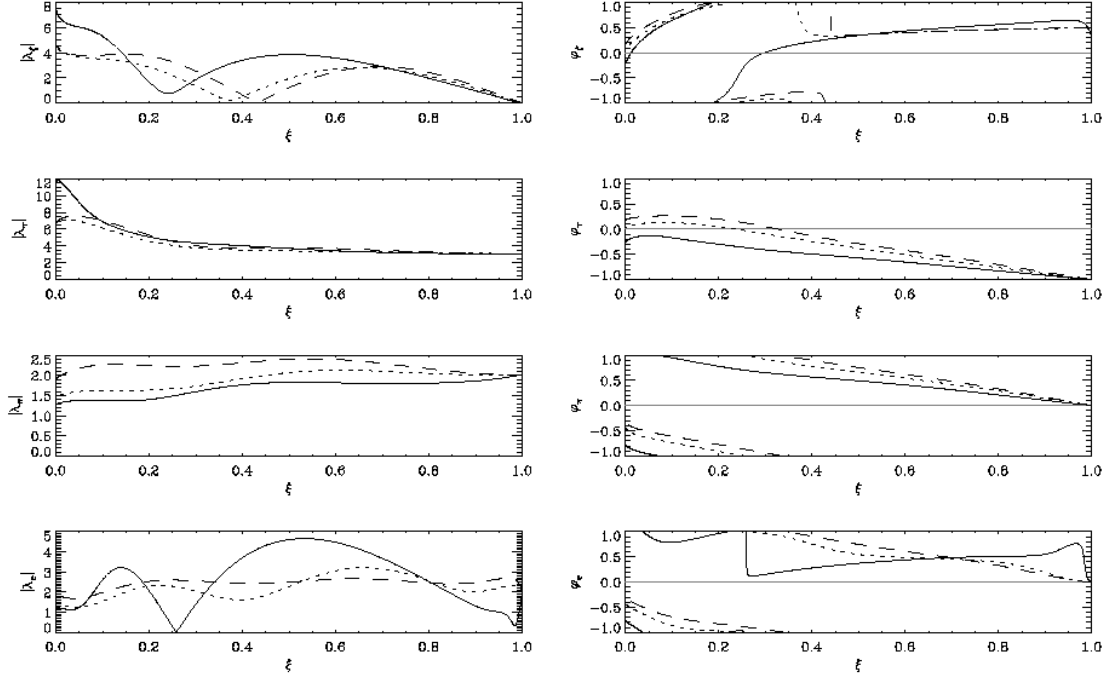


Figure B3. Same as Figure B1 but with $n = 3$ and $(\sigma_s, \psi_{ei}) = (0.2, 0.1)$.

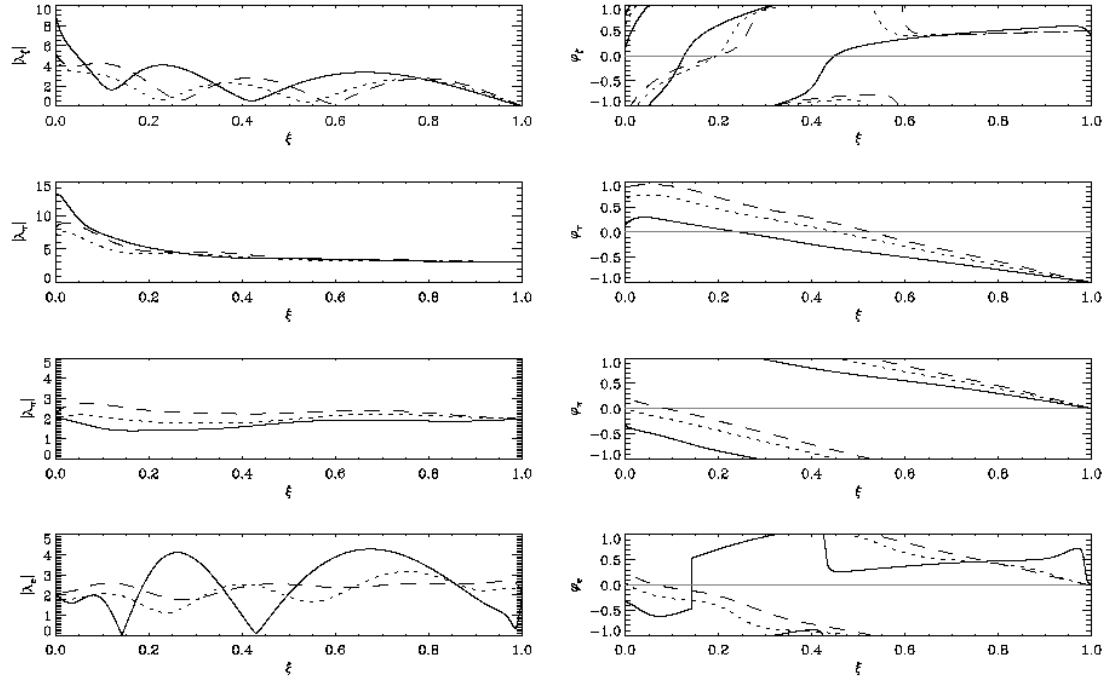


Figure B4. Same as Figure B1 but with $n = 4$ and $(\sigma_s, \psi_{ei}) = (0.2, 0.1)$.

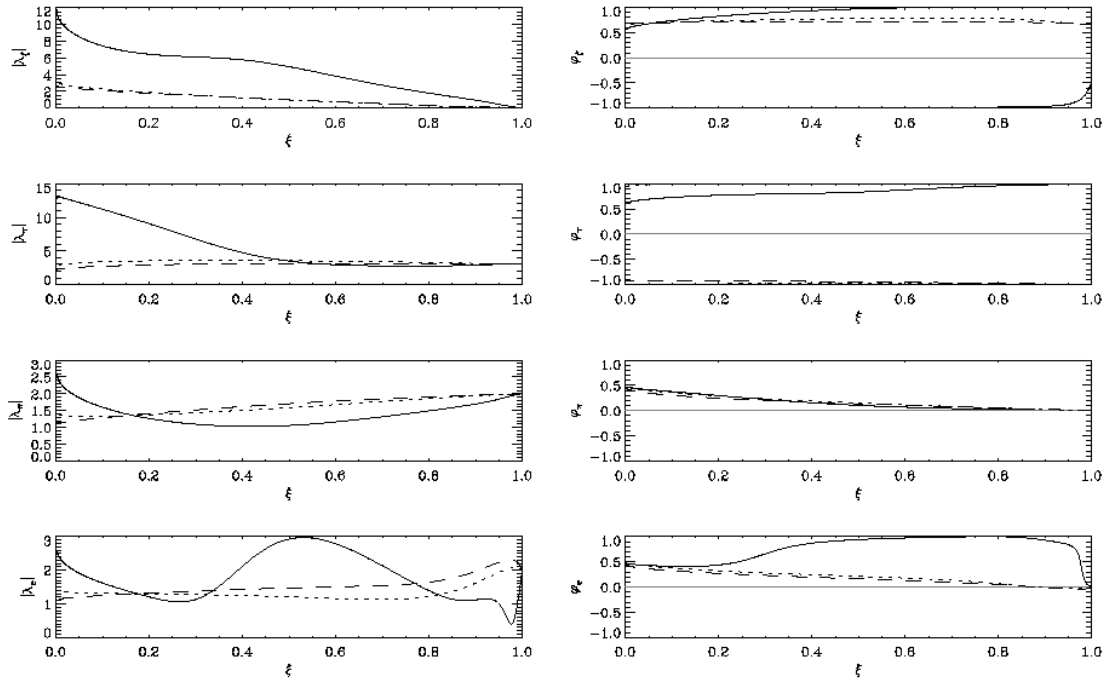


Figure B5. Same as Figure B1 but with $n = 1$ and $(\sigma_s, \psi_{ei}) = (0.5, 0.5)$.

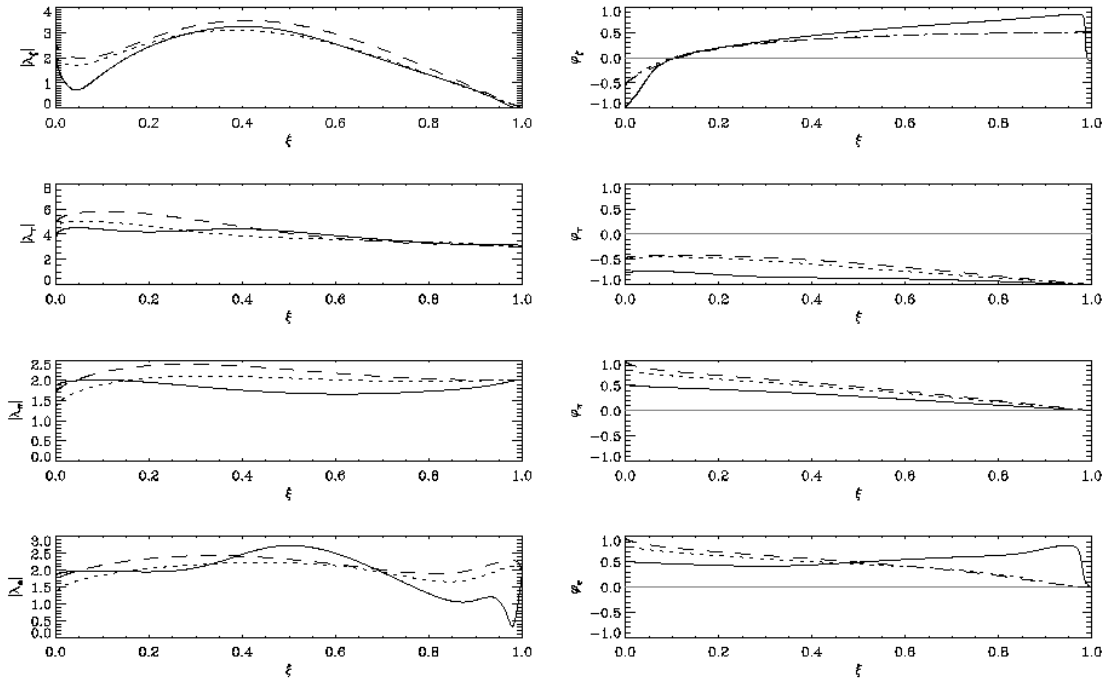


Figure B6. Same as Figure B1 but with $n = 2$ and $(\sigma_s, \psi_{ei}) = (0.5, 0.5)$.

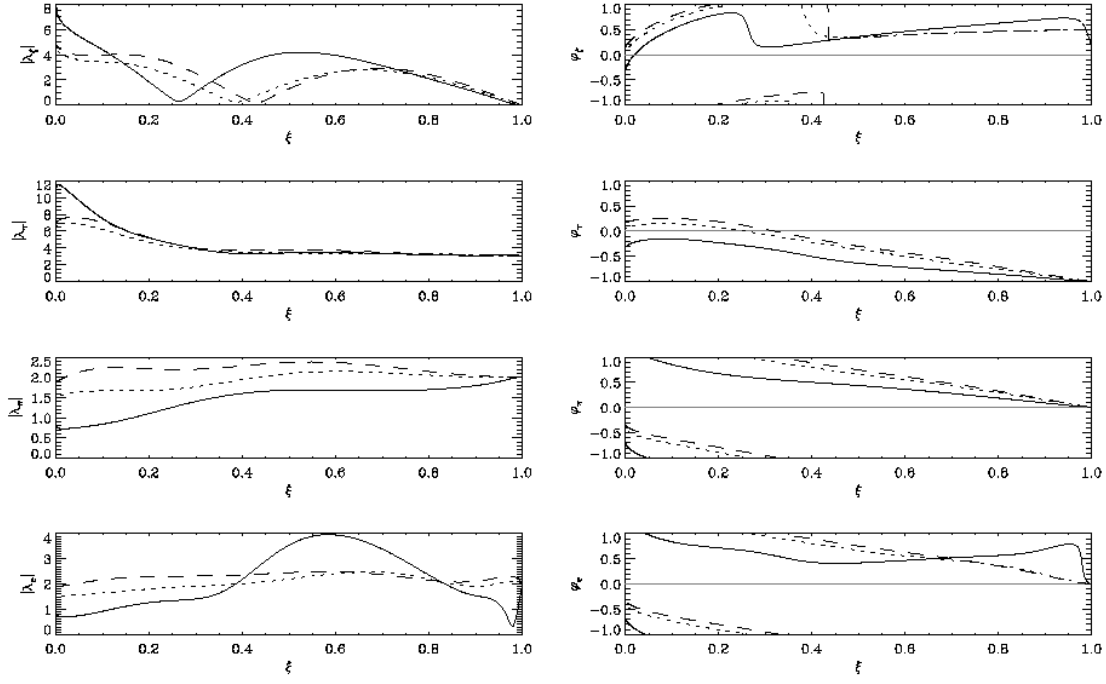


Figure B7. Same as Figure B1 but with $n = 3$ and $(\sigma_s, \psi_{ei}) = (0.5, 0.5)$.

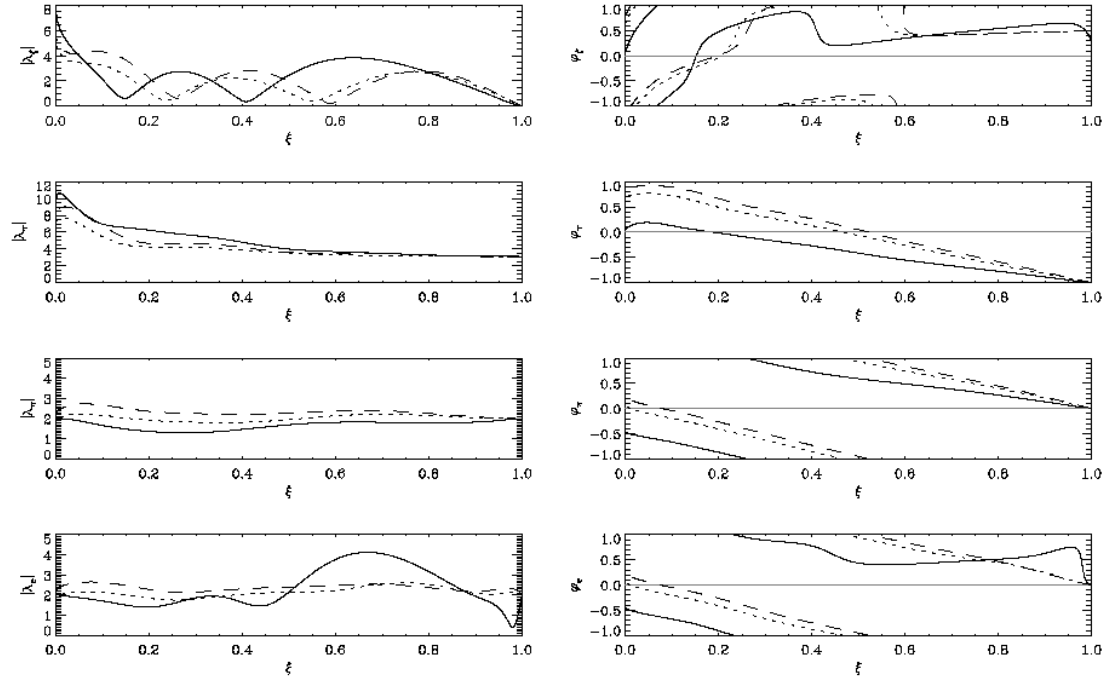


Figure B8. Same as Figure B1 but with $n = 4$ and $(\sigma_s, \psi_{ei}) = (0.5, 0.5)$.

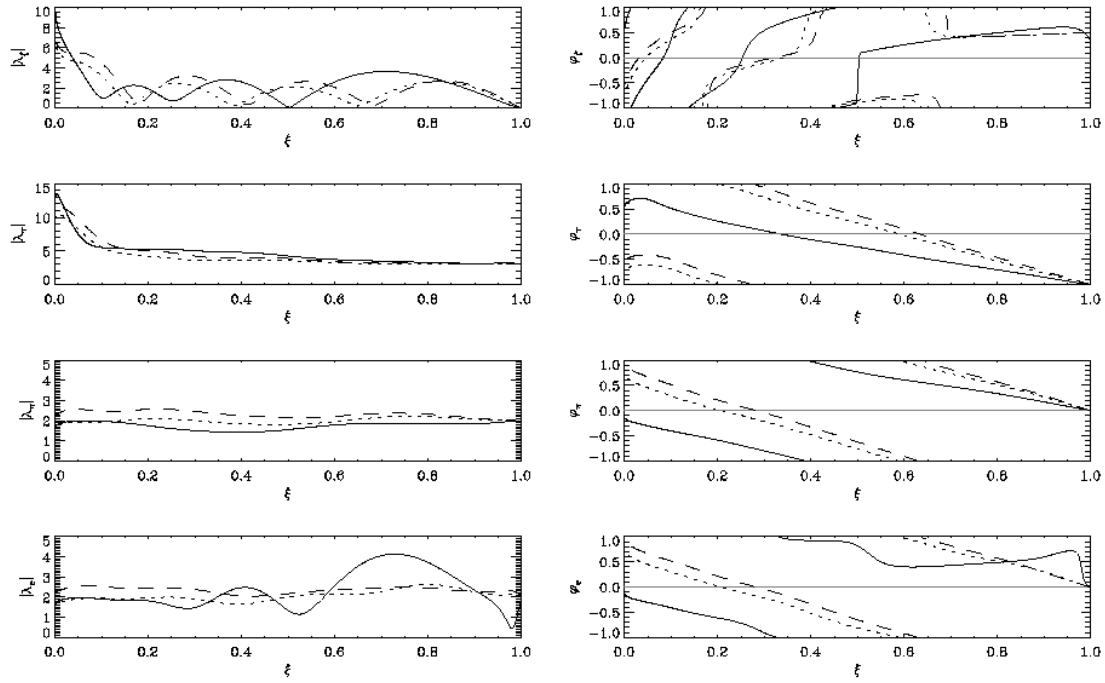


Figure B9. Same as Figure B1 but with $n = 5$ and $(\sigma_s, \psi_{ei}) = (0.5, 0.5)$.

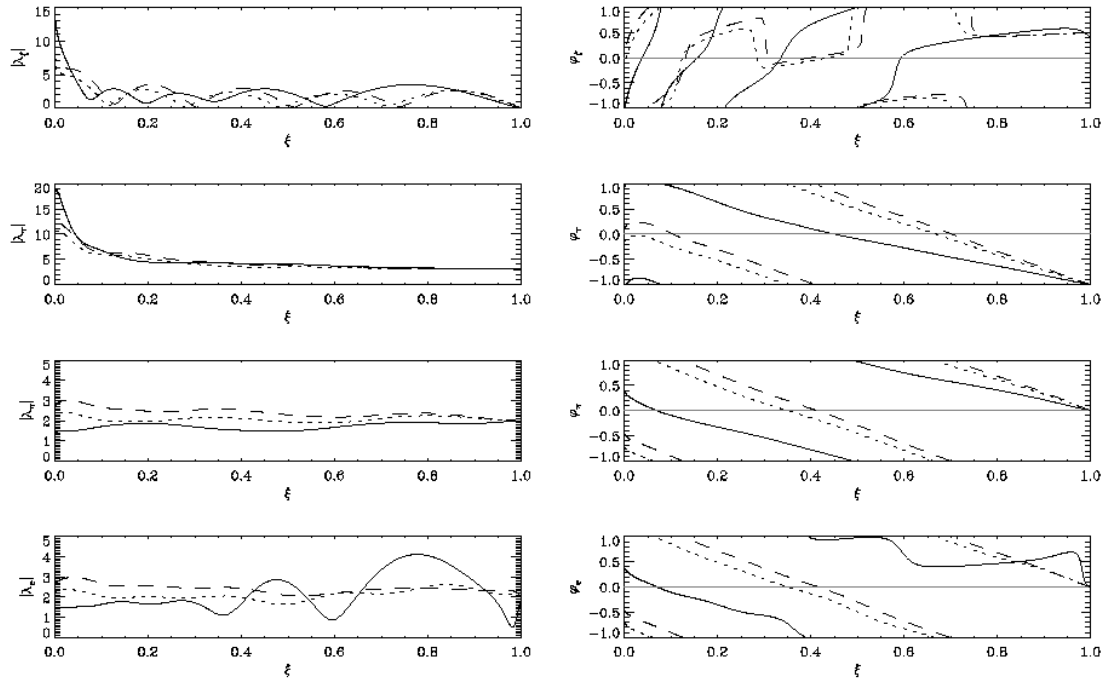


Figure B10. Same as Figure B1 but with $n = 6$ and $(\sigma_s, \psi_{ei}) = (0.5, 0.5)$.